Trends in measured and modeled lower stratospheric Antarctic vortex ozone over the past two decades

Lucien Froidevaux[1], Michael J. Schwartz[2], Douglas E. Kinnison[3], Nathaniel J. Livesey[2], Gloria L. Manney[4], Michelle L. Santee[2], William G. Read[2], and Ryan L. Fuller[2]

[1]Retired
[2]Jet Propulsion Laboratory, California Institute of Technology, Pasadena, California, USA
[3]NSF National Center for Atmospheric Research (NSF NCAR), Boulder, Colorado, USA
[4]NorthWest Research Associates, New Mexico Institute of Mining and Technology, Socorro, New Mexico, USA

Correspondence to: Michael.J.Schwartz@jpl.nasa.gov

Abstract. We analyze 2004 to 2023 winter/spring lower stratospheric Antarctic ozone data from the Aura Microwave Limb Sounder (MLS), along with similarly sampled profiles from two simulations from the Whole Atmosphere Community Climate Model (WACCM) run with specified dynamics. One of these simulations uses fixed surface organic halogens from 1998 onward. The interannual variability in MLS vortex-average ozone is well matched by WACCM, although WACCM shows a slightly smaller seasonal decrease. Probability density functions of vortex ozone profiles reveal slow increases in the smallest values; WACCM shows good agreement with MLS distribution shifts and simple linear trends. We also use multivariate linear regression with two periodic functions and a proxy for polar stratospheric clouds to derive trends in vortex-average ozone during September and October. Calculated trends are consistent with slow Antarctic vortex ozone recovery from the impact of ozone-depleting substances, with values between ~5 and 16 ppbv yr^{-1} in the 56–100 hPa layer. WACCM results agree well with those from MLS. The simulation with fixed surface organic halogens is consistent with zero trend. We also apply the Match technique, which follows MLS-observed parcels along trajectories to estimate vortex-average chemical ozone loss. Match estimates also show slow reductions in seasonal

Antarctic ozone loss, although few of the Match results represent greater than two-sigma departures from zero. Our work confirms the emergence of ozone recovery, a key goal of the Aura mission, and underscores the importance of the 1987 Montreal Protocol and its Amendments in curtailing emissions of ozone-depleting substances.

© 2026 California Institute of Technology. Government sponsorship acknowledged.

1 Introduction

Early warnings were made in the 1970s (Molina and Rowland, 1974) regarding threats to the Earth's stratospheric ozone (O_3) layer from the decomposition of chlorofluorocarbons (CFCs) emitted at the surface by industrial activities. There were human health implications from increased ultraviolet (UV) radiation at the surface, which would arise from a reduction in UV absorption by stratospheric ozone. The subsequent discovery (Farman et al., 1985) of the recurring winter/spring ozone hole development over Antarctica has made polar ozone the subject of particularly intense studies. The 1987 Montreal Protocol and its subsequent Amendments curtailed the surface emissions of ozone-depleting substances (ODSs). The following decades saw a large increase in the database of polar (and global) ozone observations, as well as in the understanding of the main causes of this phenomenon and its evolution (e.g., Solomon, 1999; Chipperfield, Santee, et al., 2022). In the polar regions, lower stratospheric ozone is destroyed during the cold winter and spring after the release of active chlorine from its stratospheric reservoir species (mainly HCl and $ClONO_2$), via heterogeneous chemical reactions enabled on the surfaces of polar stratospheric clouds (PSCs); chlorine and bromine species both contribute to the ozone destruction that peaks in September and October, after the return of sunlight to the polar regions.

As mentioned in recent Ozone Assessment Reports (WMO, 2018; WMO, 2022), a consensus has been building that, after a significant slowdown in global decreases of lower stratospheric and total column ozone abundances, we are now in the phase of ozone recovery from the effects of ODSs. The post-2000 period has been characterized by a decline in equivalent effective stratospheric chlorine (EESC), a metric used to represent the combined impact of total stratospheric chlorine and bromine abundances (Newman et al., 2007; Engel et al., 2018). EESC is related, in turn, to ODS emission changes at the surface; Lickley et al. (2024) have recently assessed how and why the estimates of EESC and global ozone recovery dates have evolved over the past two decades. There has been growing evidence for the emergence of lower stratospheric Antarctic ozone healing, although lower stratospheric ozone trends are hard to detect at other latitudes, including in the Arctic region, where larger dynamical variability occurs. Signs of the emergence of Antarctic ozone recovery since about the turn of the 21st century, following global decreases in ODSs, have been reported in analyses of a variety of data sets, including in situ data, satellite-based profiles and column ozone, coupled with model or data assimilation studies (e.g., Solomon et al., 2016; de Laat et al., 2017; Weber et al., 2018; Strahan et al., 2018; Pazmiño et al., 2018; Chipperfield, Santee, et al., 2022). Antarctic ozone profiles from ozonesondes and satellites showed that very small ozone abundances occurred seasonally after 1987, with destruction processes "saturating," that is, insensitive to further increases in ODSs because there was no more ozone to destroy. Occurrences of near-zero ozone reached a maximum at the turn of the century, after which there were decreases in the saturation of ozone loss (Kuttippurath et al., 2018; Chipperfield, Santee, et al., 2022). Quoting the latter reference, new results since 2018 support the findings that "the Antarctic ozone hole has generally diminished in size and depth since the year 2000." More recent work by Pazmiño et al. (2023) employs a model-based passive ozone tracer

and total ozone column observations since 1989 to analyze Antarctic ozone recovery based on three different metrics: maximum ozone loss at the end of winter, the onset dates for ozone loss, and a residual method that is coupled to regression analyses tied to the volume of PSCs (VPSC). Their study confirms the ozone recovery in the Antarctic, despite the increased interannual variability in the last decade compared to earlier periods. Also, according to Strahan et al. (2018), mid-September is when stratospheric ozone over Antarctica shows the largest sensitivity to decreasing ODSs and when Antarctic ozone recovery rates are strongest and most easily detected. The rate of decrease in Antarctic ozone is steepest in September; in October, there are more dynamically induced perturbations to the vortex, before its eventual breakup, typically in November or December.

For this work, we rely upon 20 years of ozone profiles retrieved from Aura Microwave Limb Sounder (MLS) measurements inside the Antarctic vortex, as detailed in Section 2. Measurements of global ozone as well as the variability in temperature and chemical processing inside the Arctic and Antarctic stratospheric vortices have been obtained nearly continuously by MLS since the Aura launch in July 2004 (e.g., Santee et al., 2005, 2011, 2024; Manney et al., 2011, 2023; Kuttippurath et al., 2015). By using this unique, continuous, well-sampled and stable ozone dataset, having the same regular data coverage over time, we avoid potential trend uncertainties that could arise from a merged record combining multiple datasets obtained using different measurement techniques with different spatio-temporal coverage within the analysis period. Two decades of high-quality MLS data provide a record of sufficient length for trend analysis. Moreover, we select abundance profiles obtained within the Antarctic vortex. This vortex-centered analysis takes into account variations in the dynamical characteristics (e.g., size, shape, and position) of the Antarctic vortex and thus better isolates the effects of chemical depletion in the

ozone hole than the use of geographic latitude bins, which inevitably mix inside-vortex and midlatitude air. We compare the MLS data to results from two simulations from the Whole Atmosphere Chemistry Climate Model (WACCM), both using specified dynamics, but one of them having surface ODSs fixed at 1998 levels; after 4–5 years, the fixed-ODS conditions lead to nearly invariant EESC levels in the polar stratosphere. In Section 3, we analyze Antarctic ozone distributions from MLS and the WACCM simulations, with a focus on Probability Density Functions (PDFs) and simple linear trends; the use of these detailed PDFs for weekly data analyses from both MLS and similarly sampled model simulations is a novel approach for Antarctic ozone studies. In addition, we comment briefly on the observed and modeled HCl and HNO_3 distributions inside the Antarctic vortex. Trends in September and October vortex-average ozone profiles are then quantified using Multivariate Linear Regression (MLR), to obtain better fits to the time series and reduce the resulting trend uncertainties. To further motivate this work and distinguish it from past results, we also discuss another metric, namely trends in Antarctic ozone loss over the period from 2005 to 2023 computed using the Match technique, which follows a multitude of air parcels inside the winter/spring lower stratospheric Antarctic vortex to diagnose chemical ozone loss (Livesey et al., 2015). We provide some discussion and conclusions in Section 4.

2 Description of datasets and model simulations

2.1 MLS data

The observations of stratospheric ozone by Aura MLS provide the backbone for this work. Aura is in a near-polar sun-synchronous orbit, and the MLS antenna scans the atmosphere vertically in front of the spacecraft from the surface to ~90 km every 24.7 s. MLS obtains atmospheric composition profiles of various species, along with temperature and cloud ice profiles, based on

day and night thermal emission measurements near 118, 190, 240, and 640 GHz, and (for parts of the mission) near 2.5 THz. Waters et al. (2006) describe the MLS measurement technique. Read et al. (2006) provide information regarding the simulated MLS forward model and related spectra. The MLS Level 2 retrievals (Livesey et al., 2006) use the optimal estimation approach (Rodgers, 2000); there is no assumption of atmospheric homogeneity along the line of sight (see Livesey and Read, 2000). These retrievals provide nearly 3500 daily profiles for temperature and for each species, day and night, from 82ºS to 82ºN, with regular temporal and spatial sampling. The MLS data used here are from the version 5 software (Livesey et al., 2022); the standard ozone product is retrieved from the MLS measurements near 240 GHz. Specifics of MLS data characterization and data quality, along with estimated errors and related information, are described by Livesey et al. (2022). We follow all the standard recommendations for data screening. The vertical resolution for ozone profiles is about 2.7 km in the vertical range considered here. Typical single-profile precision estimates for ozone, based on MLS radiance noise, range from 0.02 ppmv in the lowermost stratosphere to 0.2 ppmv at 1 hPa. Estimates of systematic errors were obtained by modeling the impact of individual error sources (e.g., calibration and spectroscopic uncertainties) on the MLS ozone profiles; an accuracy of 5–10% can be expected in the lower stratosphere, consistent with the typical agreement between MLS ozone and correlative datasets (e.g., Froidevaux et al., 2008; Jiang et al., 2007; Livesey et al., 2008). Comparisons of various satellite and ground-based ozone measurements by Hubert et al. (2016) have demonstrated that the MLS capability for detection of vertically resolved ozone trends is among the best in terms of both stability and daily coverage. Furthermore, differences between stratospheric ozone columns from MLS and the Aura Ozone Monitoring Instrument (OMI) show no significant drift (Ziemke et al., 2019). We also note that the recently released version 6 (v6) MLS data changed very little in

comparison to v5 data in the lower stratosphere for the species considered here, so significant differences in the results shown here would not be expected if the v5 data were replaced by v6 data.

2.2 Model simulations

For comparison with 20 years of MLS Antarctic polar vortex winter/spring lower stratospheric observations, we have sampled two runs of the Whole Atmosphere Community Climate Model version 6 (WACCM6) at MLS observation times and locations. The first model scenario used here is based on historical forcings (and recent updates) from the Climate Model Intercomparison Project – Phase 6 (CMIP6; Meinshausen et al., 2017). The forcings include greenhouse gases (CH_4, N_2O, and CO_2) and organic halogens. After 2014, the greenhouse gas and organic halogen inputs follow the CMIP6 SSP5-8.5 scenario that projects inputs beyond 2014 (O'Neill et al., 2016; Riahi et al., 2017; Meinshausen et al., 2020). The second simulation differs from the first only by using fixed surface organic halogens at 1998 levels, which leads to stable EESC values within ~4–5 years in the polar stratosphere. In this work, these runs will be denoted as WACCM and WACCM-fix-EESC (or WACCM-fix, for short, in the figures), respectively.

WACCM6 is a component of the Community Earth System Model (CESM) version 2.2 (Gettelman et al., 2019; Danabasoglu et al., 2020). WACCM6 uses a "high-top" set of 70 model levels between the surface and the lower thermosphere (~140 km). The model has a horizontal resolution of 0.95° latitude × 1.25° longitude. WACCM6 includes representations of boundary layer processes, shallow convection, liquid cloud macrophysics, and cloud microphysics. The chemical scheme includes the O_x, NO_x, HO_x, ClO_x, and BrO_x families, along with CH_4 and its degradation products, as well as primary non-methane hydrocarbons and related oxygenated organic compounds (Emmons et al., 2020). Reaction rates follow the JPL Publication 19-5

recommendation (Burkholder et al., 2019). The chemical scheme includes a total of 231 species and 583 chemical reactions broken down into 150 photolysis reactions, 403 gas-phase reactions, 13 tropospheric, and 17 stratospheric heterogeneous reactions. The photolytic reactions are based on both inline chemical modules and a lookup table approach (Kinnison et al., 2007).

To accurately represent polar stratospheric temperature and winds, the simulations are run in the 'specified dynamics' (SD) mode. The model dynamical constraints are taken from meteorological fields provided by the Modern-Era Retrospective Analysis for Research and Applications version 2 (MERRA-2; Gelaro et al., 2017). The MERRA-2 fields, i.e., zonal and meridional winds and temperature, are first regridded to the model horizontal and vertical grids. The model nudging (Davis et al., 2022) is updated at every (30 min) time step using the closest 3-hourly MERRA-2 fields; nudging timescales are set at 12 hours for WACCM6. Both model simulations in this study use identical MERRA-2 meteorological fields and subsequently represent identical dynamical variability. The 11-year solar cycle variability is taken from the Naval Research Laboratory's (NRL) Solar Spectral Irradiance model, version 2 (NRLSSI2; Coddington et al., 2016). WACCM6 incorporates geomagnetic variability that affects the flux of energetic particles precipitating into the atmosphere, ionizing or dissociating major species. Ion-pair production rates (IPR) by galactic cosmic rays, solar protons, and medium-energy electrons are also prescribed, following Matthes et al. (2017). The IPR rates are converted into rates of production for odd-hydrogen and odd-nitrogen species following Jackman et al. (2009). Volcanic SO_2 emissions (used in sulfate aerosol density calculations) are derived for significant volcanic eruptions using the Neely and Schmidt (2016) database updated through the year 2022.

The polar heterogeneous chemistry module that is important for this work is discussed in Wegner et al. (2013), Solomon et al. (2015), Wilka et al. (2021), and Weimer et al. (2023). The

Wegner et al. study used Aura MLS observations of Antarctic HNO_3 and H_2O and PSC distributions from the Cloud-Aerosol Lidar with Orthogonal Polarization (CALIOP) on the Cloud-Aerosol Lidar and Infrared Pathfinder Satellite Observation (CALIPSO) satellite. The CALIOP observations showed that in both polar regions, PSCs throughout the entire winter are mainly a mixture of nitric acid trihydrate (NAT) particles and supercooled ternary solution (STS) droplets. Typical WACCM assumptions about PSC formation at a given NAT supersaturation did not produce such a population of mixed particles and led to earlier removal of HNO_3 from the gas phase compared to Aura MLS observations. Wegner et al. (2013) updated the model's polar stratospheric chemistry scheme, allowing only a fraction of the total available HNO_3 to freeze to NAT, with the remaining HNO_3 forming STS, forcing the formation of mixed PSCs in the model. With this approach, both NAT and STS were present throughout the model polar winter, and the observed gas-phase polar HNO_3 abundance was better represented. Solomon et al. (2015) found that the updated heterogeneous chemistry approach recommended by Wegner et al. (2013) is strongly temperature dependent, where a degree or two difference can cause large changes in chemical reactivity and PSC surface area densities. Therefore, it is necessary to run WACCM6 in specified dynamics mode when comparing with observed ozone depletion.

PSCs not only activate chlorine through heterogeneous chemical processing but also denitrify the atmosphere through removal of HNO_3 from the gas phase and subsequent sedimentation (e.g., Solomon, 1999). Removing HNO_3 reduces the abundance of NO_2, which, in turn, enhances active chlorine (ClO) by reducing $ClONO_2$ formation rates, thus affecting ozone destruction. Initial comparisons of simulated ozone profiles to both ozonesondes and MLS showed that the model's standard approach with a NAT number density (N_{NAT}) of 0.01 cm^{-3} (Wegner et al., 2013) was not denitrifying enough. A lower N_{NAT} corresponds to larger individual particles and leads to more

denitrification by increasing the particles' settling velocities. Wilka et al. (2021) found that adopting a value of N_{NAT} of ~10^{-5} cm^{-3} resulted in the closest match to observed ozone profiles over a wide vertical range and also matched the MLS HNO_3 abundances better than other values. A more detailed analysis of the choice of N_{NAT} was conducted by Weimer et al. (2023). That study compared PDFs of modeled $ClONO_2$, ozone, and HNO_3 within the polar vortex with data from the Michelson Interferometer for Passive Atmospheric Sounding onboard the Environmental Satellite (MIPAS/Envisat), which operated between 2002 and 2012. Weimer et al. used the maximum difference between the WACCM and MIPAS cumulative density functions to check whether the distributions were distinguishable in a statistical sense. To identify the impact of NAT on the distributions of the above-mentioned species, Weimer et al. (2023) performed sensitivity simulations varying N_{NAT} between 10^{-2} and 10^{-5} cm^{-3} and concluded that a value of N_{NAT} equal to 5×10^{-4} cm^{-3} best represented the denitrification parameterization for WACCM. This value is used in the present study.

3 Analyses and results

3.1 Antarctic ozone changes and related Probability Density Functions

The Antarctic vortex edge is defined using a height-dependent threshold of scaled potential vorticity (Lawrence et al., 2018). Specifically, the Antarctic vortex edge at each level is determined from the climatological average over April through November of the maximum PV gradient as a function of equivalent latitude (the latitude that would enclose the same area between it and the pole as a given PV contour, Butchart and Remsberg, 1986). A constant value at each level is used because applying any widely used vortex edge identification method (including those based on PV gradients such as this one) on a daily basis commonly leads to large spurious

variations from day to day that may compromise comparisons of different dates and seasons (e.g., Manney et al., 2007; Lawrence and Manney, 2018; Lawrence et al., 2018).

Figure 1 shows, for each year of MLS data from 2005 to 2024, time series from austral early winter through spring of weekly vortex-average differences from each year's respective July 1-10 baseline; only a minor amount of ozone loss generally occurs before July, as evidenced by the grey shades in June and July. In Figure 2, we show the same vortex-average changes over the winter/spring for the (standard) WACCM simulation used in this work. The MLS data show that several years (2006, 2008, 2014, 2020, 2021, 2023, and 2024) have lower average values in October, after most of the chemical loss has occurred, especially in the lower portion of the vortex. Although WACCM generally shows slightly smaller ozone changes from baseline than MLS in September and October, the measured and modeled patterns of interannual variability are similar. The correlation between ozone losses and minimum temperatures in the lower stratospheric Antarctic vortex has been noted before (e.g., Kuttippurath et al., 2015; Roy et al., 2024). We discuss the correlation between temperature and ozone in the Antarctic vortex further below in the context of MLR fits to the MLS vortex-average ozone time series from 2005 to 2023.

Figure 3(a) shows the climatological distribution of weekly average MLS ozone values from early-June to late-November for the period 2005–2023, and the difference between WACCM and MLS results is seen in Fig. 3(b). The largest decreases in lower stratospheric Antarctic ozone occur during August and September (e.g., Chipperfield, Santee, et al., 2022; Strahan and Douglass, 2018; Santee et al., 2024). Indeed, Fig. 3(a) shows that changes in MLS ozone occur mostly at pressures larger than 20 hPa after early to mid-August, with effects of downward transport visible in the contours at smaller pressures. The upper region is where the WACCM values are smaller than the MLS abundances, possibly because the multi-year average downward transport velocities are too

small in the model; this conjecture seems to be qualitatively confirmed by a similar plot (not shown here) for N_2O, indicating that WACCM N_2O values are larger than MLS N_2O in the relevant height range. Some of the absolute differences may also come from systematic errors in the MLS data, since systematic uncertainties are as large as 5–15% (Livesey et al., 2022). In the main region of chemical destruction after early September, the WACCM values tend to be larger than MLS data by about 100 ppbv, or ~25% (Fig. 3(b)). Fig. 3(c) shows that WACCM O_3 mixing ratios at 68 hPa are ~300 ppbv lower than those observed by MLS in June and July but end up on the higher end in October, implying somewhat smaller modeled seasonal ozone loss than is observed; a systematic bias between modeled and measured ozone would not produce this different behavior in the slope of the ozone change.

Fig. 3(d) shows the slopes of linear fits to the time series of vortex-average ozone from MLS and both WACCM simulations at 68 hPa for 2004 to 2023. The trend estimates track well between MLS and WACCM, with positive trends typically between about 5 and 16 ppbv yr^{-1}, depending upon the date (weekly average) in winter or spring; the trends from MLS and WACCM both peak in mid-September. However, the trends obtained from the WACCM-fix-EESC simulation are consistent with a trend value of zero, as one might expect from such a fixed-EESC scenario. The seasonal patterns of changes in WACCM and MLS-derived trends are generally consistent throughout the winter/spring season from 147–14.7 hPa (not shown). The differences between WACCM and WACCM-fix-EESC trends are largest at 68.1 hPa and lose significance in this analysis by 14.7 hPa. At levels other than 68.1 hPa, there is generally more departure of the WACCM-fix-EESC trends from zero, likely reflecting the impact of changes in dynamics that are generally consistent among WACCM, WACCM-fix-EESC and MLS. More sophisticated ozone trend analyses are pursued in Sect. 3.2.

Figure 4 depicts PDFs for vortex-average ozone (panels a, c, and e) and related trends in these distributions (panels b, d, and f) for the week centered on September 12. Panels a, c and e all have sharply peaked distributions up to 83 hPa, with the broader distributions at 68–18 hPa reflecting larger spatial and/or interannual variability in lower stratospheric ozone. WACCM generally has slightly larger values than those of MLS at these levels. WACCM also lacks the near-zero values seen in the tail of the MLS PDF at 83–26 hPa, where MLS has observed some cases of early near-complete ozone depletion. At 68–46 hPa, the MLS single-observation precision is ~half of the width of a 100-ppmv histogram bin, so the MLS points near zero do not merely reflect random noise. The WACCM-fix-EESC distribution at these levels also has more of the lowest (100–200 ppbv) ozone values than the standard WACCM simulation, suggesting less recovery, as implied also by Fig. 3(d); a larger value for EESC would indeed qualitatively account for such a difference between the two model simulations.

The right side of Fig. 4 shows how the PDFs tend to change over time (from 2005 to 2023), with both MLS and WACCM showing shifts in the peaks of the distributions over the 20-year record, with fewer occurrences of values below 500 ppbv (green and blue areas on the left edge of panels (b) and (d)) and more at 800 ppbv and higher (brown areas of panels (b) and (d)). Bins without black stippling have trends with magnitudes more than twice the uncertainty in the fitted values. PDF trends for WACCM-fix-EESC in Figure 4(f) show no shift from lower to higher values at 68-18 hPa, but rather an apparent tightening of the PDF, with brown sandwiched between green where panels (b) and (d) show such a shift. Figure 5 helps to visualize this shift by comparing the MLS PDFs at 38 and 82 hPa for a week in mid-September in two five-year periods at the beginning (2004–2008, in blue) and end (2019–2023, in red) of the study period; in the later years, the peak of the distributions has clearly shifted towards larger abundances, and there are almost no

ozone values below 500 ppbv. This result is consistent with work by Kuttippurath et al. (2018), who demonstrated decreasing saturation in lower stratospheric Antarctic ozone loss. However, if we consider a week in mid-October, results show only subtle changes in the MLS PDF trends (Fig. S1); the ozone values are too small (and perturbed) during this period to allow for a robust trend detection.

Figure 6 shows MLS HCl in the same format as for O_3 in Fig. 3. MLS shows highly depleted climatological HCl abundances during winter for pressures larger than 20 hPa, with a sharp increase at the end of September towards values between 2.5 and 3 ppbv in the spring (Fig. 6(a)). The differences in Fig. 6(b) indicate that WACCM has HCl values that are slightly larger in the winter but recover in the spring to mean values that are slightly smaller than those observed by MLS, as shown also at 68 hPa in Fig. 6(c), where modeled HCl does not quite reach 2.5 ppbv at the end of November. The Antarctic early-winter discrepancy between HCl rates of decrease from models and from MLS has been addressed recently by Grooss et al. (2025), who point out that additional chemical mechanisms involving Cl_2O_2, HOOCl, and HOCl could resolve this issue, although there is a need for more laboratory validation regarding the reaction rates of these postulated mechanisms. The fact that WACCM has somewhat less HCl in the polar spring may in part reflect a total inorganic chlorine (Cly) value that is slightly low, possibly because of a deficit in very short-lived substances (VSLSs) and some inaccuracies in repartitioning during chlorine deactivation. Fig. 6(d) shows linear trends of about −0.02 ppbv yr^{-1} for vortex-average MLS HCl in late spring, when 68.1 hPa HCl abundances (~2.8 ppbv) are comparable to mid-to-upper stratospheric HCl values. These trends correspond to about −0.7% yr^{-1}, which is somewhat larger than global trends (since the turn of the century) in upper stratospheric HCl of about −0.3 to −0.5%

321 yr^{-1} (WMO, 2022). In contrast, the WACCM-fix-EESC simulation leads to HCl trend results that
322 are consistent with zero trend, as one would expect.

323 Figure 7 is analogous to Figs. 3 and 6, but for modeled and observed HNO_3. Strong depletion
324 of gaseous HNO_3 is observed in the climatology from MLS (panel (a)), with the WACCM
325 simulation (panel (b)) showing slightly larger values than the MLS abundances in early winter and
326 slightly lower values in the spring. As mentioned in Sect. 2.2, this WACCM fit to Antarctic HNO_3
327 observations is clearly better than that in previous simulations from WACCM, following
328 improvements in the modeled heterogeneous chemical processing scheme. In Fig. 7(d), the MLS
329 and modeled linear trends in HNO_3 from 2005 to 2023 all agree very well, with near-zero trend
330 for most months. During June and July, a negative trend is apparent in MLS data as well as in the
331 model simulations. Investigation of the underlying cause of these apparent trends in early-winter
332 HNO_3 is beyond the scope of this study.

333 **3.2 Further analyses of trends in Antarctic vortex ozone**

334 **3.2.1 MLR analyses of vortex-average ozone trends**

335 Here, we use 7-day means of Antarctic vortex-average ozone abundances for 2005–2023 to
336 perform multivariate linear regression analyses to produce better fits to the time series and reduce
337 the error bars compared to a fit with only a linear trend term (and a constant term). We apply the
338 same analyses to both model simulations.

339 The main regression model used here has two sets of periodic functions, both described by sine
340 and cosine terms, with period 1 and period 2 representing, respectively, a short-term and a decadal-
341 type component. Our standard run has a 2.5-yr periodicity for period 1, since we observe (see
342 further below) that most Antarctic time series exhibit short-term variability. Moreover, the quasi-

343 biennial oscillation (QBO) is a well-studied phenomenon in the Earth's stratosphere (e.g., Baldwin
344 et al., 2001; Anstey et al., 2022) that can be represented by such a periodicity; there is evidence of
345 QBO influence on Antarctic temperature and inorganic chlorine (and thus ozone) over Antarctica
346 (Strahan et al., 2014; Strahan and Douglass, 2018). We should note that using a 2- or 3-yr
347 periodicity for period 1, rather than 2.5 yr, does not lead to major changes in terms of our trend
348 results, given the typical trend uncertainties. We have also varied period 2 (see further below), but
349 our standard retrieval uses a value of 11 years, which can represent solar cycle variability, even if
350 this may not be the main cause of decadal-type variability in Antarctic ozone. The other terms in
351 the MLR analysis are a constant and a linear (trend) term.

352 Also, we use a proxy term tied to the region within the vortex with temperatures allowing the
353 possible existence of polar stratospheric clouds (PSCs). The volume (VPSC) of air that is exposed
354 to temperatures below T_{NAT}, the threshold for existence of nitric acid trihydrate (NAT) PSCs, has
355 been shown to be well correlated with springtime ozone loss in the polar vortices (e.g., Rex et al.,
356 2004; Tilmes et al., 2004). Although it is known that liquid-phase particles play a large role in the
357 destruction of polar ozone, the T_{NAT} threshold is often used as a first-order estimate of the
358 conditions necessary for significant chemical ozone destruction inside the polar vortex. To
359 describe the proxy we use for the VPSC term, we show in Figure 8 the area with temperatures
360 below T_{NAT} and the area of the vortex exposed to sunlight (Lawrence et al., 2015; Lawrence et al.,
361 2018), since sunlight is required for the photochemical processes involved in Antarctic vortex
362 ozone destruction (see the review by Solomon, 1999). In Figure 8(a) and 8(d), the areas (expressed
363 as a fraction of the SH hemisphere area) from different potential temperature levels (from 330 K
364 to 620 K) are averaged to obtain a lower stratospheric layer-average area, which is akin to a
365 summation (or volume, VPSC). The second variable represents the lower stratospheric layer-

366 average sunlit vortex area (also as a fraction of the SH hemisphere area) , which is then multiplied
367 by VPSC. This product (Figure 8, right-hand panels) is used as a proxy term (labeled $VPSC_{sun}$ in
368 the fitting function below) for our MLR analysis of ozone vortex-average abundances. The 2019
369 vortex was significantly perturbed by a September sudden stratospheric warming event, leading to
370 an anomalously small Antarctic vortex and column ozone destruction (e.g., Wargan et al., 2020;
371 Roy et al., 2024). Figure 8 shows that the lower stratospheric layer-average vortex area with
372 temperatures below T_{NAT} drops much faster in 2019 (panel (a)) than in a representative year like
373 2022 (see panel (d)); this also affects the time-averaged (mean from April 1 to date) layer-average
374 diagnostic values (thick lines) in September and October, as well as the final proxy values in panels
375 (c) and (f), even if the averaged effect is dampened compared to the daily values (thin lines).
376 The MLR time series function to be fitted for coefficients a, b, c_n, d_n, and f has the following
377 form:
378 $$y(t) = a + b\,(t - t_m) + \sum_n \left(c_n \sin 2\pi t/P_n + d_n \cos 2\pi t/P_n \right) + f\,VPSC_{sun}(t)$$
379 with the yearly time series values expressed by time (t); t_m refers to the series mid-point, and the
380 linear trend term is coefficient b. The sine and cosine functions provide for periodic variations
381 with periods P_n. As mentioned above, we use two periods in the MLR equation—a short-term
382 (QBO-type) period (P_1) and a longer-term (decadal-type) period (P_2); in a sensitivity study
383 discussed later, we add a term relating to the Antarctic Oscillation.
384 In Figure 9, we show examples of the year-to-year relative changes in the lower stratospheric
385 $VPSC_{sun}$ proxy from 2005–2023 for the week centered on September 19, along with the vortex-
386 average ozone abundances from MLS for that week. As indicated by the values of the correlation
387 coefficient (R), there is an anti-correlation between mean ozone and the $VPSC_{sun}$ proxy; for
388 example, the 2019 vortex, with its larger-than-usual ozone values in late September, shows a

positive peak, whereas the proxy indicates a low value for that year. An expanded view of this correlation coefficient versus pressure level for various weeks in September and October is provided in Figure 10, which shows that the anti-correlation between ozone and $VPSC_{sun}$ grows between early September and late October, when the cumulative impact of chemical ozone destruction peaks. To first order, we expect that a polar vortex winter/spring with lower-than-average temperatures will lead to more chemical processing and larger chemical ozone destruction, with relatively smaller vortex-average ozone values in the spring.

In Figure S2, we show that use of longer periods (9 to 11 yr) for P_2 enables the MLR analysis to explain a larger fraction of the variance at pressures between 56 and 100 hPa, in comparison to 4- to 8-yr periods; choices of 9, 10, or 11 yr do not lead to very different correlations. We have chosen to use 11 yr for our standard MLR retrievals. The 11-yr solar cycle can impact ozone through standard photochemistry (related to solar ultraviolet flux) or energetic particle precipitation (EPP) (e.g., Gordon et al., 2021). EPP can have a direct impact on ozone in the upper stratosphere and mesosphere, as well as indirect effects from downward transport of nitrogen oxides to lower altitudes, although the likely long-term impact of EPP on lower stratospheric Antarctic ozone is difficult to ascertain (Maliniemi et al., 2022). However, we note that the phase of the solar cycle itself does not agree with the typical phase of the proxy term that we derive from the MLR fits. The correlation between the 11-yr fitted component and the solar cycle variation itself changes with pressure, with a range of positive, negative, or near-zero correlations; elucidating a causal relationship would require modeling that is beyond the scope of this paper. Transport variability is another factor that can modulate Antarctic vortex ozone abundances (e.g., Kessenich et al., 2023). More generally, there is evidence for multi-year variability and hemisphere-dependent changes in HCl (Mahieu et al., 2014) and HNO_3 (Strahan et al., 2020), with

changes in the circulation invoked as a likely driver; these variations could also influence the variability in Antarctic ozone. Some transport-related variability is included in the $VPSC_{sun}$ proxy through the influence of temperatures and vortex area. However, we focus on winter/early spring periods when chlorine and bromine chemical effects are at their strongest over the well-isolated lower stratospheric Antarctic vortex.

We show in Figure S3 the same plots as in Fig. S2, but for P_1, the 2.5-yr period we have used in our standard MLR fits. As one might expect, the fraction of variance explained by the short-term period does not have sensitivity to the value of P_2. This is shown mainly to contrast the R^2 values from P_1 with those from P_2. For 56 and 68 hPa, the P_2 term explains more of the variance in the ozone time series, whereas the short-term period explains more of the variance at 82 and 100 hPa.

We have applied the MLR analysis described above, including the $VPSC_{sun}$ variability term, to the MLS-derived Antarctic vortex-average values from different September and October weeks over 2005–2023. Examples of the ozone time series and the fits are shown in Fig. 11 at 68 and 100 hPa for the week centered on September 19. Both the linear component (slope of the fit) and the full fit to the time series are shown; as expected, much better results are obtained with the full fit. Figure 12 compares the overall results at 68 hPa for the MLR-based MLS vortex-average ozone trends in September and October to the trends obtained from simple linear regression. Although the trends themselves do not change very much, the trend error bars are significantly reduced in the MLR case (panel (a)); on average, there is a 20–25% reduction in the error bars, with a reduction of ~40% at 121 hPa and ~10% at 46 hPa. In Figure 12(b) and 12(c), we also show how diagnostics of the fit quality change between these two regression methods. The MLR fits, in comparison to simple linear trend analysis, yield much larger correlation coefficients (0.8 to 0.95

435 rather than 0.4 to 0.5) and smaller RMS residuals (by a factor of 30–50%). Figure S4 provides the
436 same information for 100 hPa, with similarly improved results for the MLR case.

437 Figure 13 shows the MLR-based trends for 2005–2023 at 46, 68, and 100 hPa for MLS and the
438 two WACCM simulations of Antarctic vortex ozone (sampled following the MLS viewing
439 pattern). We find that some of these lower stratospheric Antarctic vortex-average ozone trends in
440 September and October are significantly different from zero (taken here to mean further from zero
441 than the 2σ error bar) for pressures larger than 50 hPa. For example, the mid-September to early
442 October MLS ozone trends (black points) are significantly different from zero at 68 and 100 hPa.
443 Typical September MLS trends are ~15 ppbv yr^{-1} at 68 hPa and ~7 ppbv yr^{-1} at 100 hPa, while
444 October trends at these two levels are mostly between zero and 10 ppbv yr^{-1}. The WACCM
445 simulation (red points) generally matches the MLS results quite well, although the error bars are
446 slightly larger. Also, as for MLS, most of the WACCM trends in October are not significantly
447 different from zero. The WACCM-fix-EESC simulation (blue points) yields lower stratospheric
448 ozone trends that are consistent with zero, as one might expect from a fixed-EESC scheme. We
449 provide in Figs. 14 and 15, respectively, the correlation coefficients and the RMS residuals, as
450 introduced in Fig. 12 for MLS, for the results from MLS, WACCM, and WACCM-fix-EESC at
451 46, 68, and 100 hPa. At 68 and 100 hPa, the R values typically lie between 0.8 and 0.95 for MLS
452 and WACCM, with slightly lower values for WACCM-fix-EESC. Correlation coefficients are
453 somewhat lower in general at 46 hPa, a region where the trends are most often found to be not
454 significant. The variation of the WACCM RMS residuals as a function of pressure follows that
455 obtained for MLS; there is not much variation in these, or in the R values, as a function of the
456 September and October dates.

We also provide another way of roughly estimating the changes that occur in winter/spring inside the Antarctic vortex, by taking the differences (ΔO_3) between the vortex-average ozone values in September or October and the mean vortex ozone values from the first week in July, before substantial chemical ozone loss has occurred, especially in the lower stratosphere, where the positive trends are most significant. This approach is commonly employed to partially mitigate the effects on ozone arising from transport-related variability. For example, Strahan et al. (2019) used this methodology and noted that the majority of ozone loss occurs after early July. Figure 16 gives trends in the lower stratosphere for the MLS, WACCM, and WACCM-fix-EESC cases; values are close to and consistent with the results in Fig. 13, which considers the actual ozone values rather than differences from an early winter baseline.

Figure 17 provides a summary of the MLS, WACCM, and WACCM-fix-EESC Antarctic vortex-average ozone trend profiles in the lower stratosphere for each of the September and October weeks that we analyzed, with triangles marking trends found to be significantly different from zero. The trends for MLS and WACCM that are significantly different from zero are all positive, with September trends of order 5–15 ppbv yr^{-1} peaking at 68 hPa and with somewhat smaller trends (5–10 ppbv yr^{-1}) in October, which usually brings more perturbed conditions as the vortex weakens.

For pressures larger than 50 hPa, the analyses of 75°S–82°S zonal mean MLS daily data from 2004 to 2022 by Kessenich et al. (2023) also show some significant positive trends of 10–20 ppbv yr^{-1} in September. Similarly, positive (and significant) September trends of 15–30 ppbv yr^{-1} are obtained for 2001–2023 in this pressure range by He et al. (2026), who recently analyzed zonal mean values in the broader 60°S–90°S region from the chemistry transport model TOMCAT. Wang et al. (2025) obtained significant September vortex-average trends in MLS ozone of 15–20

ppbv yr^{-1} in the same pressure range for a shorter time period (2005–2018), but this trend would probably have been slightly smaller if the period under consideration had included more of the recent years with a colder than usual lower stratospheric vortex.

For pressures less than 50 hPa, significant mean September trend values in vortex-average ozone obtained by Wang et al. (2025) peak at ~40 ppbv yr^{-1} (near 20–30 hPa). These trends are significantly larger than our weekly mean MLS September trend results at those pressures (with trends peaking at ~20 ppbv yr^{-1} but generally not significant). This apparent discrepancy in derived ozone trends is likely largely attributable to differences in the analysis periods used. Also, the 20–30 hPa (~540–620 K, ~22–25 km) layer, which lies just above the region of strongest chemical processing in the heart of the ozone hole, is subject to large interannual variability in the relative interplay between dynamical and chemical effects in September and October. Thus, as illustrated in Fig. S5, it is particularly sensitive to the interval chosen (both start and end dates) for ozone trend estimation; trend uncertainties are also large in this region. At pressures smaller than 50 hPa, the WACCM simulation with fixed EESC gives results that scatter about zero and are generally not significantly different from zero, although there are a few significantly negative values in late October that might be associated with transport-related changes during the more dynamically perturbed conditions. Indeed, even the MLS (panel (a)) and WACCM (panel (b)) results show more variability in the mid-stratosphere, with some non-significant negative late-October trend values. For this region, Kessenich et al. (2023) obtained significant (and large) negative October trends, mostly in the range of –50 to –100 ppbv yr^{-1}. These authors have argued that negative trends in October could be the result of a slight delay in the ozone hole spring break up as a function of year. The TOMCAT trends obtained by He et al. (2026) in this pressure range are also negative in October, with values between about –30 and –80 ppbv yr^{-1}; the earlier starting year (2021) used

503 by these authors could lead to some differences in results. Also, Wang et al. (2025) point out that
504 ozone trends over Antarctica are shifted towards zero or more negative trends if zonal-mean polar
505 ozone data are used rather than vortex averages.

506 In addition, we tested a regression including a term for the variability that arises at high southern
507 latitudes in connection with the Antarctic Oscillation (AAO), which characterizes atmospheric
508 mass and pressure changes between the southern midlatitudes and the Antarctic region (e.g., Gong
509 and Wang, 1999). More information on the estimation of the AAO index can be found at
510 https://www.cpc.ncep.noaa.gov/. The AAO appears to have several multi-year variability
511 components, including a periodicity of about 6 years and other longer-term periodicities (Zhang et
512 al., 2010). If we add the winter/spring average AAO index changes as a function of year to the
513 previously described regression fits, the results are similar to and consistent with the MLR results
514 for MLS, WACCM, and WACCM-fix-EESC shown above, both in terms of trends and their
515 corresponding error bars (Fig. S6). The addition of such an AAO proxy does not substantially
516 change the total explained variance or the RMS residuals of the fits (not shown).

517 Finally, we comment briefly on the upper stratospheric Antarctic vortex from our simple linear
518 trend analyses, as MLR analyses including a VPSC proxy are not appropriate for that region.
519 Essentially no significant upper stratospheric trends are found for the three weeks in September
520 considered (Fig. S7). The October trends (not shown) are most often not significant in the lower
521 stratosphere and have even more scatter in the upper stratosphere, where MLS and both WACCM
522 simulations show a negative but generally not significant trend. Dynamical changes may be the
523 reason for this behavior, further analysis of which is beyond the scope of this study.

3.2.2 Ozone loss trends from Match analyses of MLS data

We now turn to an ozone trend analysis that focuses more specifically on the winter/spring chemical ozone losses inside the Antarctic vortex and better accounts for transport-related changes, including descent across pressure surfaces or leakage into or out of the vortex. The so-called Match technique was pioneered by von der Gathen et al. (1995), who used multiple ozonesonde profiles within the Arctic vortex to quantify chemical ozone loss. This methodology has been applied (e.g., Livesey et al., 2015; Santee et al., 2024) to Aura MLS ozone within the polar winter vortices; chemical ozone loss is estimated by tracking a multitude of observed parcels using trajectory calculations along potential temperature surfaces and matching the parcels to subsequent MLS measurements during winter and spring.

Figure S8 shows daily cumulative ozone losses for each year from 2005 to 2023 from Match results inside the Antarctic vortex during May to October at four different potential temperature levels between 350 K and 700 K; given that noise in these calculations leads to positive and negative changes in May and June, we focus on the net negative changes (chemical losses), which typically occur after July 1. In October, there can be a slight turnaround in the cumulative changes, as the vortex becomes more affected by mixing across its boundary. The Match profiles of maximum (cumulative) Antarctic ozone loss, which typically occurs in early October (although the date does change from year to year), are shown in Figure 18. Chemical losses as large as 4 ppmv are obtained in some of the early years of the Aura mission. As we already mentioned, the well-known September perturbation in 2019 led to some of the weakest ozone destruction in the MLS record, as can also be seen in these plots, where the 2019 maximum lower stratospheric loss only reaches ~2.5 ppmv. The loss values here are slightly different (and generally larger) than the Match-based losses reported by Santee et al. (2024); for the most part, these differences are caused

by our use of maximum losses in Fig. 18, rather than calculating the cumulative chemical changes over fixed start and end dates as done by Santee et al., and we also use a more conservative threshold (10% vs. 25%) for the allowed magnitude of along-trajectory PV variability.

We then use the ozone loss values for different dates in September and October to calculate weekly average losses, as we did for earlier analyses presented here. A time series example of the inferred chemical losses from 2005 to 2023 for the week centered on September 19 is provided in Figure S9, along with a simple linear fit to that series; the positive trend indicated by this linear fit implies smaller chemical losses over time. Figure 19 shows that, while these linear fits lead to some positive trends in the lower part of the Antarctic vortex, there are also oscillations in the loss profiles, and only a few trends are significantly different from zero; we only show the error bars when the trends are deemed to be significant (i.e., further away from zero than the 2σ error values). We also show the trends obtained from fits to the maximum ozone losses from every year between 2005 and 2023; none of these trends are significantly different from zero. Given the small number of Match-derived trends with significant values, we have not pursued any other fits to these chemical ozone loss time series, as we do not expect greater significance from more elaborate MLR fits. The few significant trends obtained from this Match analysis agree, to first order, with the linear trends obtained from our analyses of vortex-average ozone (see the September linear trends in Fig. 12, which are all between 15 and 20 ppbv yr^{-1}). A layer-average of all the September Match trends in chemical ozone loss for potential temperatures below 600 K is slightly less than 10 ppbv yr^{-1} (not shown), which is somewhat smaller than the September vortex-average trends obtained in the previous section.

4 Discussion and Conclusions

Aura MLS measurements of ozone and other species have played a prominent role in the characterization of global stratospheric change since 2004. Here, we have analyzed the MLS distributions of lower stratospheric Antarctic vortex-average ozone profiles from June to November, along with similarly sampled profiles from two WACCM simulations, driven by MERRA-2 meteorological fields with realistic dynamical and temperature information. One of these simulations uses a scheme with surface ODS emissions fixed at 1998 values. These chemistry-climate model simulations include effects from downward transport within the vortex, temperature changes and related changes in PSC activity and heterogeneous chemistry, solar flux and EPP variations, and slow changes in greenhouse gas abundances. Wang et al. (2025) have pointed out that Antarctic ozone changes arising from reductions in ODSs should dominate the impacts from greenhouse gases, for now.

The interannual variability in MLS-derived weekly averaged ozone abundances inside the Antarctic vortex is generally well matched by WACCM, although the magnitude of the winter-to-spring ozone decrease is typically slightly smaller in the model. Analyses of probability density functions of ozone profile distributions inside the lower stratospheric Antarctic vortex from 2004 to 2023 reveal shifts as a function of year; in particular, there are some relative decreases in the bins with the smallest ozone abundances. The standard WACCM simulation shows similar shifts and good overall agreement with MLS in lower stratospheric vortex-average ozone linear trends from July to November. Such shifts are qualitatively consistent with past findings of changes in ozone loss saturation over Antarctica (Kuttippurath et al., 2018), based mainly on sonde profile data (and partly on MLS data). The fixed-EESC simulation from WACCM shows no significant trends in lower stratospheric ozone and HCl, as one might expect. We also include MLS and

WACCM Antarctic vortex profile comparisons for HNO_3; these show good agreement and no significant trends, except for a negative trend in June-July that requires further investigation.

As has been commented on previously (WMO, 2022), differences in the various approaches used to quantify Antarctic ozone trends make comparisons of trend estimates from different studies problematic. We note that recent Antarctic vortex analyses by Chang et al. (2025) lead to lower stratospheric vortex-average trends of 10 ppbv yr^{-1} in mid-to-late September and 7 ppbv yr^{-1} in early October, based on MLS ozone data from 2005 to 2022; this is in good accord with our analyses from 2005 to 2023, both in absolute value and in the sense that October shows smaller trends than September, as has been shown previously (WMO, 2022). Other recent Antarctic trend results (see Sect. 3.2.1) show broad agreement with the positive September trends obtained here for pressures larger than 50 hPa; however, more detailed investigations into some of the larger differences are beyond the scope of this work.

We also used multivariate linear regression fits to weekly mean lower stratospheric vortex-average ozone profiles from MLS and the two WACCM simulations to calculate trends during September and October, when the fastest chemical destruction of ozone occurs. It is useful to analyze both the absolute ozone abundances and the seasonal changes (from early July) in our trend analyses, since both diagnostics should ultimately show robust signs of recovery from the effect of diminishing ODSs. A metric relating to the volume of the sunlit vortex with temperatures low enough to enable NAT PSC formation explains a large part of the year-to-year variability in MLS vortex-average ozone observations. Other proxies used in the regression include two sets of cosine and sine functions with periods of 2.5 and 11 years to represent effects from the quasi-biennial oscillation and longer-term variations, such as the solar cycle (possibly in relation to particle precipitation) or the Antarctic Oscillation; these proxies showed smaller individual

614 impacts on the fits. Reducing the long-term periodicity to 9 or 10 yr does not change the trend
615 results appreciably. Regardless of the exact causal links between geophysical variability and
616 Antarctic vortex ozone, we show that applying MLR analyses rather than simple linear regression
617 decreases lower stratospheric Antarctic ozone trend errors by as much as 40%, while also, as
618 expected, improving the regression fit diagnostics.

619 Overall, our results indicate that lower stratospheric Antarctic ozone values and seasonal
620 changes through mid-September to mid-October are consistent with a recovery from the impact of
621 ODSs, with significant positive trends between 5 and 16 ppbv yr^{-1} at 56 to 100 hPa; trend
622 uncertainties (2σ) range from ~8 ppbv yr^{-1} at 68–56 hPa to ~4 ppbv yr^{-1}at 100 hPa. The WACCM
623 results agree well with those from MLS. As expected, the model simulation with fixed ODS
624 emissions leads to Antarctic ozone trends in the lower stratosphere that are consistent with zero
625 trend. We estimate that the positive ozone trends we obtain for mid-September correspond to an
626 average partial lower stratospheric (pressures larger than 46 hPa) column change of 1 to 1.5 DU
627 yr^{-1}. These values are within the range of Antarctic total column ozone change (~25–30 DU
628 between 2000 and 2025, or ~1–1.2 DU yr^{-1}) obtained from various models (e.g., Dhomse et al.,
629 2018; Amos et al., 2020). However, partial column ozone changes of this magnitude are still less
630 than half of the amount needed for ozone to return to pre-ozone-hole values over Antarctica, which
631 models predict will occur shortly after mid-century (WMO, 2022).

632 Finally, we explored trends in chemical ozone loss as quantified by the Match technique,
633 whereby MLS measurements of ozone are tracked along trajectories to estimate vortex-average
634 chemical ozone loss during winter/spring. While the Match results show some reductions in
635 seasonal lower stratospheric Antarctic chemical ozone loss over the 2005 to 2023 period,
636 consistent with a positive trend (based on simple linear regression) of order

637 5–15 ppbv yr^{-1}, we obtain statistical significance (as defined in this work) for only a limited subset
638 of cases in mid-to-late September. However, many of the lower stratospheric Match results are
639 consistent with a zero trend; there is also a large spread in these trend results as a function of height
640 (potential temperature) inside the vortex. We do not expect that use of a more sophisticated
641 regression fit would produce much improvement in the significance of trends in chemical ozone
642 loss, given the values of the linear-only regression trends and their error bars.

643 These analyses represent new facets of the characterization of the recovery of Antarctic vortex
644 ozone as ODSs diminish, which has been a key goal of the Aura mission. Our results support the
645 robust detection of significant recovery in lower stratospheric Antarctic ozone during parts of
646 September and October over the 2005–2023 period, at pressures larger than 50 hPa. This work
647 adds to the body of evidence underscoring the importance of the 1987 Montreal Protocol and its
648 Amendments, as this international agreement has been a shining example of how policymakers
649 around the world can come together to solve a global environmental problem. However, the
650 upcoming dearth of daily global height-resolved stratospheric composition measurements after the
651 end of the Aura mission (Salawitch et al., 2025) will greatly hinder the ability to detect and
652 understand short- and longer-term changes in stratospheric composition and their effects on the
653 Antarctic ozone hole.

654

655 **Data availability.**

656 The MLS data files are publicly available from the Goddard Earth Sciences Data and Information
657 Services Center (GES DISC) at https://earthdata.nasa.gov/eosdis/daacs/gesdisc. The WACCM
658 simulation used here comes from a publicly released version of the Community Earth System
659 Model. Data from the model simulations generated for this work will be made available at the
660 following link (to be added later).

Code availability. More details to be added later regarding this.

Supplement. Supplementary material is included.

Author contributions. LF proposed and designed this project, along with (primarily) MJS and DEK; LF also led the writing of this manuscript's first few drafts, along with DEK and MJS. MJS provided analyses and results mostly for the first part of this manuscript (Sect. 3.1), using the WACCM model simulations provided by DEK. LF provided analyses and results mostly for the second part of this manuscript (Sect. 3.2). NJL played a key role in the Match analyses and the interpretation of related seasonal chemical ozone losses. GLM played a key role in the production of files with daily vortex-average quantities, used here for trend analyses. MLS provided detailed comments and helped to improve the manuscript overall. WGR, in part, provided invaluable work towards the creation of the MLS version 5 MLS data used here. RLF mostly provided technical assistance for the datasets and some of the coding used in this work.

Competing interests. The authors declare that they have no conflict of interest.

Acknowledgments. We acknowledge the work of the whole Aura MLS team (past and present) for their various contributions over the years to the mission; special thanks go to Z. D. Lawrence for his contributions to the creation of vortex-related diagnostic quantities. WACCM is a component of the CESM, supported by the National Science Foundation (NSF). We also acknowledge high-performance computing support from Cheyenne (doi:10.5065/D6RX99HX) provided by NCAR's Computational and Information Systems Laboratory, sponsored by the NSF. Work at the Jet Propulsion Laboratory, California Institute of Technology, was performed under

contract with the National Aeronautics and Space Administration (80NM0018D0004). [Copyright 2026. All rights reserved.]

Financial support. LF, MJS, and RAF were funded in part by the NASA Atmospheric Composition Modeling and Analysis Program (ACMAP). NJL, GLM, MLS, and WGR were funded, in part, by the Aura Microwave Limb Sounder project. DEK was funded by NASA and NSF grants. Part of this material is based upon work supported by the NSF National Center for Atmospheric Research, which is a major facility sponsored by the U.S. National Science Foundation under Cooperative Agreement No. 1852977.

References

Amos, M., Young, P. J., Hosking, J. S., Lamarque, J.-F., Abraham, N. L., Akiyoshi, H., Archibald, A. T., Bekki, S., Deushi, M., Jöckel, P., Kinnison, D., Kirner, O., Kunze, M., Marchand, M., Plummer, D. A., Saint-Martin, D., Sudo, K., Tilmes, S., and Yamashita, Y.:, Atmos. Chem. Phys., 20, 9961–9977, https://doi.org/10.5194/acp-20-9661-2020, 2020.

Anstey, J. A., Osprey, S. M., Alexander, J., Baldwin, M. P., Butchart, N., Gray, L., Kawatani, Y., Newman, P. A., and Richter, J. H.: Impacts, processes and projections of the quasi-biennial oscillation, Nature Reviews Earth and Environment, 3, 588–603, https://doi.org/10.1038/s43017-022-00323-7, 2022.

Baldwin, M. P., Gray, L. J., Dunkerton, T. J., Hamilton, K., Haynes, P. H., Randel, W. J., Holton, J. R., Alexander, M. J., Hirota, I., Horinouchi, T., Jones, D. B. A., Kinnersley, J. S., Marquardt, C., Sato, K., and Takahashi, M.: The quasi-biennial oscillation, Rev. Geophys., 39, 179–229, https://doi.org/10.1029/1999RG000073, 2001.

Burkholder, J. B., Sander, S. P., Abbatt, J. P. D., Barker, J. R., Cappa, C., Crounse, J. D., Dibble, T. S., Huie, R. E., Kolb, C. E., Kurylo, M. J., Orkin, V. L., Percival, C. J., Wilmouth, D. M., and Wine, P. H.: Chemical kinetics and photochemical data for use in atmospheric studies, Evaluation No. 19, JPL Publication 19-5, Jet Propulsion Laboratory, California Institute of Technology, Pasadena, http://jpldataeval.jpl.nasa.gov (last access: 1 December 2022), 2019.

Butchart, N., and Remsberg, E. E.: The area of the stratospheric polar vortex as a diagnostic for tracer transport on an isentropic surface. Journal of the Atmospheric Sciences, 43(13), 1319–1339, https://doi.org/10.1175/1520-0469(1986)043<1319:taotsp>2.0.co;2, 1986.

Chang, J. H.-W., Pien, C. H., Sentian, J., Cordero, R. R., Ooi, M. C.-G., and Wong, Y. J.: Evidence of localized H_2O increases and O_3 recovery in the Antarctic lower stratospheric vortex: MLS observations and BDC variability during late winter to spring, Atmos. Res., 328, 108248, https://doi.org/10.1016/j.atmosres.2025.108428, 2025.

Chipperfield, M. P., Santee, M. L., et al.: Chapter 4, World Meteorological Organization (WMO). Scientific Assessment of Ozone Depletion: 2022, GAW Report No. 278, 509 pp., WMO, Geneva, ISBN: 978-9914-733-97-6, 2022.

Coddington, O., Lean, J., Pilewskie, P., Snow, M., and Lindholm, D.: A solar irradiance climate data record, B. Am. Meteo- rol. Soc., 97, 1265–1282, https://doi.org/10.1175/BAMS-D-14- 00265.1, 2016.

Danabasoglu, G., Lamarque, J. F., Bacmeister, J., Bailey, D. A., DuVivier, A. K., Edwards, J., Emmons, L. K., Fasullo, J., Garcia, R., Gettelman, A., Hannay, C., Holland, M. M., Large, W. G., Lauritzen, P. H., Lawrence, D. M., Lenaerts, J. T., Lind- say, K., Lipscomb, W. H., Mills, M. J., Neale, R., Oleson, K. W., Otto-Bliesner, B., Phillips, A. S., Sacks, W., Tilmes, S., van Kampenhout, L., Vertenstein, M.,

728 Bertini, A., Dennis, J., Deser, C., Fischer, C., Fox-Kemper, B., Kay, J. E., Kinnison, D., Kushner, P. J.,
729 Larson, V. E., Long, M. C., Mickelson, S., Moore, J. K., Nienhouse, E., Polvani, L., Rasch, P. J., and
730 Strand, W. G.: The Community Earth System Model Version 2 (CESM2), J. Adv. Model. Earth Syst.,
731 12, e2019MS001916, https://doi.org/10.1029/2019MS001916, 2020.
732 Davis, N. A., Callaghan, P., Simpson, I. R., and Tilmes, S.: Specified dynamics scheme impacts on wave-
733 mean flow dynamics, convection, and tracer transport in CESM2 (WACCM6), Atmos. Chem. Phys.,
734 22, 197–214, https://doi.org/10.5194/acp-22-197-2022, 2022.
735 de Laat, A. T. J., van Weele, M., and van der A, R. J.: Onset of stratospheric ozone recovery in the Antarctic
736 ozone hole in assimilated daily total ozone columns, J. Geophys. Res., 122, 11,880–11,899,
737 https://doi.org/10.1002/2016JD025723, 2017.
738 Dhomse, S. S., Kinnison, D., Chipperfield, M. P., Salawitch, R. J., Cionni, I., Hegglin, M. I., Abraham, N.
739 L., Akiyoshi, H., Archibald, A. T., Bednarz, E. M., Bekki, S., Braesicke, P., Butchart, N., Dameris, M.,
740 Deushi, M., Frith, S., Hardiman, S. C., Hassler, B., Horowitz, L. W., Hu, R.-M., Jöckel, P., Josse, B.,
741 Kirner, O., Kremser, S., Langematz, U., Lewis, J., Marchand, M., Lin, M., Mancini, E., Marécal, V.,
742 Michou, M., Morgenstern, O., O'Connor, F. M., Oman, L., Pitari, G., Plummer, D. A., Pyle, J. A.,
743 Revell, L. E., Rozanov, E., Schofield, R., Stenke, A., Stone, K., Sudo, K., Tilmes, S., Visioni, D.,
744 Yamashita, Y., and Zeng, G.: Estimates of ozone return dates from Chemistry-Climate Model Initiative
745 simulations, Atmos. Chem. Phys., 18, 8409–8438, https://doi.org/10.5194/acp-18-8409-2018, 2018.
746 Emmons, L. K., Schwantes, R. H., Orlando, J. J., Tyndall, G., Kinnison, D., Lamarque, J.-F., Marsh, D.,
747 Mills, M. J., Tilmes, S., Bardeen, C., Buchholz, R. R., Conley, A., Gettelman, A., Garcia, R., Simpson,
748 I., Blake, D. R., Meinardi, S., and Pétron, G.: The Chemistry Mechanism in the Community Earth
749 System Model version 2 (CESM2), J. Adv. Model. Earth Syst., 12, e2019MS001882,
750 https://doi.org/10.1029/2019MS001882, 2020.
751 Engel, A., Bönisch, H., Ostermöller, J., Chipperfield, M. P., Dhomse, S., and Jöckel, P.: A refined method
752 for calculating equivalent effective stratospheric chlorine, Atmos. Chem. Phys., 18, 601–
753 619, https://doi.org/10.5194/acp-18-601-2018, 2018.
754 Farman, J. C., Gardiner, B. G., and Shanklin, J. D.: Large losses of total ozone in Antarctica reveal seasonal
755 ClOx/NOx interaction, Nature, 315, 207–210, 1985.
756 Froidevaux, L., Jiang, Y. B., Lambert, A., Livesey, N. J., Read, W. G., Waters, J. W., Browell, E. V., Hair,
757 J. W., Avery, M. A., McGee, T. J., Tiwgg, L. W., Sumnicht, G. K., Jucks, K. W., Margitan, J. J., Sen,
758 B., Stachnik, R. A., Toon, G. C., Bernath, P. F., Boone, C. D., Walker, K. A., Filipiak, M. J., Harwood,
759 R. S., Fuller, R. A., Manney, G. L., Schwartz, M. J., Daffer, W. H., Drouin, B. J., Cofield, R. E., Cuddy,
760 D. T., Jarnot, R. F., Knosp, B. W., Perun, V. S., Snyder, W. V., Stek, P. C., Thurstans, R. P., and Wagner,

P. A.: Validation of Aura Microwave Limb Sounder stratospheric and mesospheric ozone measurements, J. Geophys. Res., 113, D15S20, doi:10.1029/2007JD008771, 2008.

Gelaro, R., McCarty, W., Suarez, M. J., Todling, R., Molod, A., Takacs, L., Randles, C. A., Darmenov, A., Bosilovich, M. G., Reichle, R., Wargan, K., Coy, L., Cullather, R., Draper, C., Akella, S., Buchard, V., Conaty, A., da Silva, A. M., Gu, W., Kim, G.-K., Koster, R., Lucchesi, R., Merkova, D., Nielsen, J. E., Partyka, G., Pawson, S., Putman, W., Rienecker, M., Schubert, S. D., Sienkiewicz, M., and Zhao, B.: The Modern-Era Retrospective Analysis for Research and Applications, Version 2 (MERRA2), J. Clim., 30, 5419–5454, https://doi.org/10.1175/JCLI-D-16-0758.1, 2017.

Gettelman, A., Mills, M. J., Kinnison, D. E., Garcia, R. R., Smith, A. K., Marsh, D. R., Tilmes, S., Vitt, F., Bardeen, C. G., McInerny, J., Liu, H. L., Solomon, S. C., Polvani, L. M., Emmons, L. K., Lamarque, J. F., Richter, J. H., Glanville, A. S., Bacmeister, J. T., Phillips, A. S., Neale, R. B., Simp- son, I. R., DuVivier, A. K., Hodzic, A., and Randel, W. J.: The Whole Atmosphere Community Climate Model Version 6 (WACCM6), J. Geophys. Res.-Atmos., 124, 12380–12403, https://doi.org/10.1029/2019JD030943, 2019.

Gong, D., and Wang, S.: Definition of Antarctic oscillation index, Geophys. Res. Lett., 26, 4, 459-462, https://doi.org/10.1029/1999GL900003, 1999.

Gordon, E.M., A. Seppälä, B. Funke, J. Tamminen, and K.A. Walker, Observational evidence of energetic particle precipitation NOx (EPP-NOx) interaction with chlorine curbing Antarctic ozone loss, Atmos. Chem. Phys., 21, 2819–2836, doi:10.5194/acp-21-2819-2021, 2021.

Grooss, J.-U., Müller, R., Crowley, J. N., and Hegglin, M. I.: Chlorine peroxide reaction explains observed wintertime hydrogen chloride in the Antarctic vortex, Nature Commun. Earth Environ., 6, 496, https://doi.org/10.1038/s43247-025-02499-4, 2025.

He, H., Chipperfield, M. P., Dhomse, S. S., Feng, W., Chang, S., Li, Y., Weber, M., and Heddell, S.: Analysis of Antarctic ozone trends from 1979 to 2023, EGUsphere [preprint], https://doi.org/10.5194/egusphere-2026-560, 2026. [Accepted]

Hubert, D., Lambert, J.-C., Verhoelst, T., Granville, J., Keppens, A., Baray, J.-L., Bourassa, A. E., Cortesi, U., Degenstein, D. A., Froidevaux, L., Godin-Beekmann, S., Hoppel, K. W., Johnson, B. J., Kyrölä, E., Leblanc, T., Lichtenberg, G., Marchand, M., McElroy, C. T., Murtagh, D., Nakane, H., Portafaix, T., Querel, R., Russell III, J. M., Salvador, J., Smit, H. G. J., Stebel, K., Steinbrecht, W., Strawbridge, K. B., Stübi, R., Swart, D. P. J., Taha, G., Tarasick, D. W., Thompson, A. M., Urban, J., van Gijsel, J. A. E., Van Malderen, R., von der Gathen, P., Walker, K. A., Wolfram, E., and Zawodny, J. M.: Ground-based assessment of the bias and long-term stability of 14 limb and occultation ozone profile data records, Atmos. Meas. Tech., 9, 2497–2534, https://doi.org/10.5194/amt-9-2497-2016, 2016.

Jackman, C. H., Marsh, D. R., Vitt, F. M., Garcia, R. R., Randall, C. E., Fleming, E. L., and Frith, S. M.: Long-term middle atmospheric influence of very large solar proton events, J. Geophys. Res., 114, D11304, https://doi.org/10.1029/2008JD011415, 2009.

Jiang, Y. B., Froidevaux, L., Lambert, A., Livesey, N. J., Read, W. G., Waters, J. W., Bojkov, B., Leblanc, T., McDermid, I. S., Godin-Beekmann, S., Filipiak, M. J., Harwood, R. S., Fuller, R. A., Daffer, W. H., Drouin, B. J., Cofield, R. E., Cuddy, D. T., Jarnot, R. F., Knosp, B. W., Perun, V. S., Schwartz, M. J., Snyder, W. V., Stek, P. C., Thurstans, R. P., Wagner, P. A., Allaart, M., Andersen, S. B., Bodeker, G., Calpini, B., Claude, H., Coetzee, G., Davies, J., De Backer, H., Dier, H., Fujiwara, M., Johnson, B., Kelder, H., Leme, N. P., Koenig-Langlo, G., Kyro, E., Laneve, G., Fook, L. S., Merrill, J., Morris, G., Newchurch, M., Oltmans, S., Parrondos, M. C., Posny, F., Schmidlin, F., Skrivankova, P., Stubi, R., Tarasick, D., Thompson, A., Thouret, V., Viatte, P., Vomel, H., von Der Gathen, P., Yela, M., and Zablocki, G.: Validation of the Aura Microwave Limb Sounder Ozone by ozonesonde and lidar measurements, J. Geophys. Res., 112, D24S34, doi:10.1029/2007JD008776, 2007.

Kessenich, H., Seppala, A., and Rodger, C.: Potential drivers of the recent large Antarctic ozone holes, Nature Comm., 14, 1, doi:10.1038/s41467-023-42637-0, 2023.

Kinnison, D. E., Brasseur, G. P., Walters, S., Garcia, R. R., Marsh, D. R., Sassi, F., Harvey, V. L., Randall, C. E., Emmons, L., Lamarque, J. F., Hess, P., Orlando, J. J., Tie, X. X., Randel, W., Pan, L. L., Gettelman, A., Granier, C., Diehl, T., Niemeier, U., and Simmons, A. J.: Sensitivity of chemical tracers to meteorological parameters in the MOZART-3 chemical transport model, J. Geophys. Res.-Atmos., 112, 20302, https://doi.org/10.1029/2006JD007879, 2007.

Kuttippurath, J., Godin-Beekmann, S., Lefèvre, F., Santee, M. L., Froidevaux, L., and Hauchecorne, A., Variability in Antarctic ozone loss in the last decade (2004–2013): high-resolution simulations compared to Aura MLS observations, Atmos. Chem. Phys., 15, 10385–10397, doi:10.5194/acp-15-10385-2015, 2015.

Kuttippurath, J., Kumar, P., Nair, P.J., and Pandey, P.: Emergence of ozone recovery evidenced by reduction in the occurrence of Antarctic ozone loss saturation, Clim. Atmos. Sci., 1, 42 (2018). https://doi.org/10.1038/s41612-018-0052-6, 2018.

Lawrence, Z. D., and Manney, G. L.: Characterizing stratospheric polar vortex variability with computer vision techniques, J. Geophys. Res.-Atmos., 123, 1510–1535, https://doi.org/10.1002/2017JD027556, 2018.

Lawrence, Z. D., Manney, G. L., Minschwaner, K., Santee, M. L., and Lambert, A.: Comparisons of polar processing diagnostics from 34 years of the ERA-Interim and MERRA reanalyses, Atmos. Chem. Phys., 15, 3873–3892, https://doi.org/10.5194/acp-15-3873-2015, 2015.

827 Lawrence, Z. D., Manney, G. L., & Wargan, K.: Reanalysis intercomparisons of stratospheric polar
828 processing diagnostics, Atmos. Chem. Phys., 18, 13547–13579, https://doi.org/10.5194/acp-18-13547-
829 2018, 2018.
830 Lickley, M. J., Daniel, J. S., McBride, L. A., Salawitch, R. J., and Velders, G. J. M.: The return to 1980
831 stratospheric halogen levels: a moving target in ozone assessments from 2006 to 2022, Atmos. Chem.
832 Phys., 24, 13081–13099, https://doi.org/10.5194/acp-24-13081-2024, 2024.
833 Livesey, N. J., and Read, W. G.: Direct retrieval of line-of-sight atmospheric structure from limb sounding
834 observations, Geophys. Res. Lett., 27, 891-894, https://doi.org/10.1029/1999GL010964, 2000.
835 Livesey, N. J., Snyder, W. V., Read, W. G., and Wagner, P. A.: Retrieval algorithms for the EOS
836 Microwave Limb Sounder (MLS), IEEE T. Geosci. Remote, 44, 1144–1155,
837 doi:10.1109/TGRS.2006.872327, 2006.
838 Livesey, N. J., Filipiak, M. J., Froidevaux, L., Read, W. G., Lambert, A., Santee, M. L., Jiang, J. H., Waters,
839 J. W., Cofield, R. E., Cuddy, D. T., Daffer, W. H., Drouin, B. J., Fuller, R. A., Jarnot, R. F., Jiang, Y.
840 B., Knosp, B. W., Li, Q. B., Perun, V. S., Schwartz, M. J., Snyder, W. V., Stek, P. C., Thurstans, R. P.,
841 Wagner, P. A., Pumphrey, H. C., Avery, M., Browell, E. V., Cammas, J.-P., Christensen, L. E., Edwards,
842 D. P., Emmons, L. K., Gao, R.-S., Jost, H.-J., Loewenstein, M., Lopez, J. D., Nédélec, P., Osterman, G.
843 B., Sachse, G. W., and Webster, C. R.: Validation of Aura Microwave Limb Sounder O_3 and CO
844 observations in the upper troposphere and lower stratosphere, J. Geophys. Res., 113, D15S02,
845 doi:10.1029/2007JD008805, 2008.
846 Livesey, N. J., Santee, M. L., and Manney, G. L.: A Match-based approach to the estimation of polar
847 stratospheric ozone loss using Aura Microwave Limb Sounder observations, Atmos. Chem. Phys., 15,
848 9945–9963, doi:10.5194/acp-15-9945-2015, 2015.
849 Livesey, N. J., Read, W. G., Wagner, P. A., Froidevaux, L., Santee, M. L., Schwartz, M. J., Lambert, A.,
850 Millan Valle, L. F., Pumphrey, H. C., Manney, G. L., Fuller, R. A., Jarnot, R. F., Knosp, B. W., and
851 Lay, R. R.: EOS MLS Version 5.0x Level 2 and 3 data quality and description document, Tech. rep., Jet
852 Propulsion Laboratory D-105336 Rev. B, Jan. 30, 2022, https://mls.jpl.nasa.gov/eos-aura-
853 mls/documentation.php, 2022.
854 Mahieu, E., Chipperfield, M. P., Notholt, J., Reddmann, T., Anderson, J., Bernath, P. F., Blumenstock, T.,
855 Coffey, M. T., Dhomse, S. S., Feng, W., Franco, B., Froidevaux, L., Griffith, D. W. T., Hannigan, J.
856 W., Hase, F., Hossaini, R., Jones, N. B., Morino, I., Murata, I., Nakajima, H., Palm, M., Paton-Walsh,
857 C., Russell III, J. M., Schneider, M., Servais, C., Smale, D., and Walker, K.: Recent northern hemisphere
858 stratospheric HCl increase due to atmospheric circulation changes, Nature, 515(7525), 104–107,
859 https://doi.org/10.1038/nature13857, 2014.

Maliniemi, V., Arsenovic, P., Seppälä, A., and Nesse Tyssøy, H.: The influence of energetic particle precipitation on Antarctic stratospheric chlorine and ozone over the 20th century, Atmos. Chem. Phys. 22, 8137–8149, 2022.

Manney, G. L., Daffer, W. H., Zawodny, J. M., Bernath, P. F., Hoppel, K. W., Walker, K. A., and Waters, J. W.: Solar occultation satellite data and derived meteorological products: Sampling issues and comparisons with Aura Microwave Limb Sounder, J. Geophys. Res., 112 (D24), D24S50, https://doi.org/10.1029/2007JD008709, 2007.

Manney, G. L., Santee, M. L., Rex, M., Livesey, N. J., Pitts, M. C., Veefkind, P., et al.: Unprecedented Arctic ozone loss in 2011, Nature, 478(7370), 469–475, doi.org/10.1038/nature10556, 2011

Manney, G. L., Santee, M. L., Lambert, A., Millán, L. F., Minschwaner, K., Werner, F., Lawrence, Z. D., Read, W. G., Livesey, N. J., and Wang, T.: Siege in the southern stratosphere: HungaTonga–Hunga Ha'apai water vapor excluded from the 2022 Antarctic polar vortex, Geophys. Res. Lett., 50(14), e2023GL103855, https://doi.org/10.1029/2023GL103855, 2023.

Matthes, K., Funke, B., Andersson, M. E., Barnard, L., Beer, J., Charbonneau, P., Clilverd, M. A., Dudok de Wit, T., Haberreiter, M., Hendry, A., Jackman, C. H., Kretzschmar, M., Kruschke, T., Kunze, M., Langematz, U., Marsh, D. R., Maycock, A. C., Misios, S., Rodger, C. J., Scaife, A. A., Seppälä, A., Shangguan, M., Sinnhuber, M., Tourpali, K., Usoskin, I., van de Kamp, M., Verronen, P. T., and Versick, S.: Solar forcing for CMIP6 (v3.2), Geoscientific Model Development, 10(6), 2247–2302, https://doi.org/10.5194/gmd-10-2247-2017, 2017.

Meinshausen, M., Vogel, E., Nauels, A., Lorbacher, K., Meinshausen, N., Etheridge, D. M., Fraser, P. J., Montzka, S. A., Rayner, P. J., Trudinger, C. M., Krumme, P. B., Beyerle, U., Canadell, J. G., Daniel, J. S., Enting, I. G., Law, R. M., Lunder, C. R., O'Doherty, S., Prinn, R. G., Reimann, S., Rubino, M., Velders, G. J. M., Vollmer, M. K., Wang, R. H.-J., and Weiss, R.: Historical greenhouse gas concentrations for climate modelling (CMIP6), Geoscientific Model Development, 10(5), 2057–2116. https://doi.org/10.5194/gmd-10-2057-2017, 2017.

Meinshausen, M., Nicholls, Z. R. J., Lewis, J., Gidden, M. J., Vogel, E., Freund, M., Beyerle, U., Gessner, C., Nauels, A., Bauer, N., Canadell, J. G., Daniel, J. S., John, A., Krummel, P. B., Luderer, G., Meinshausen, N., Montzka, S. A., Rayner, P. J., Reimann, S., Smith, S. J., van den Berg, M., Velders, G. J. M., Vollmer, M. K., and Wang, R. H. J.: The shared socio-economic pathway (SSP) greenhouse gas concentrations and their extensions to 2500, Geosci. Model Dev., 13, 3571–3605, https://doi.org/10.5194/gmd-13-3571-2020, 2020.

Neely, R. R. and Schmidt, A.: VolcanEESM: Global volcanic sulphur dioxide (SO_2) emissions database from 1850 to present – Version 1.0., https://doi.org/10.5285/76ebdc0b-0eed-4f70-b89e-55e606bcd568, 2016.

Newman, P. A., Daniel, J. S., Waugh, D. W., and Nash, E. R.: A new formulation of equivalent effective stratospheric chlorine (EESC), https://doi.org/10.5194/acp-7-4537-2007, 2007.

O'Neill, B. C., Tebaldi, C., van Vuuren, D. P., Eyring, V., Friedlingstein, P., Hurtt, G., Knutti, R., Kriegler, E., Lamarque, J.-F., Lowe, J., Meehl, G. A., Moss, R., Riahi, K., and Sanderson, B. M.: The Scenario Model Intercomparison Project (ScenarioMIP) for CMIP6, Geosci. Model Dev., 9, 3461–3482, https://doi.org/10.5194/gmd-9-3461-2016, 2016.

Pazmiño, A., Godin-Beekmann, S., Hauchecorne, A., Claud, C., Khaykin, S., Goutail, F., Wolfram, E., Salvador, J., and Quel, E.: Multiple symptoms of total ozone recovery inside the Antarctic vortex during austral spring, Atmos. Chem. Phys., 18, 7557–7572, https://doi.org/10.5194/acp-18-7557-2018, 2018.

Pazmiño, A., Goutail, F., Sophie Godin-Beekmann, S., Hauchecorne, A., Pommereau, J.-P., Chipperfield, M. P., Feng, W., Franck Lefèvre, F., Lecouffe, A., Van Roozendael, M., Jepsen, N., Hansen, G., Rigel Kivi, R., Kimberly Strong, K., and Walker, K. A.: Trends in polar ozone loss since 1989: potential sign of recovery in the Arctic ozone column, Atmos. Chem. Phys., 23, 15655–15670, https://doi.org/10.5194/acp-23-15655-2023, 2023.

Read, W. G., Shippony, Z., and Snyder, W. V.: The clear-sky unpolarized forward model for the EOS Aura microwave limb sounder (MLS), IEEE Trans. Geosci. Remote Sens., 44, 1367-1379, https://doi.org/10.1109/TGRS.2006.862267, 2006.

Rex, M., Salawitch, R. J., von der Gathen, P., Harris, N. R. P., Chipperfield, M. P., and Naujokat, B.: Arctic ozone loss and climate change, Geophys. Res. Lett., 31, L04116, doi:10.1029/2003GL018844, 2004.

Riahi, K., van Vuuren, D. P., Kriegler, E., Edmonds, J., O'Neill, B. C., Fujimori, S., Bauer, N., Calvin, K., Dellink, R., Fricko, O., Lutz, W., Popp, A., Crespo Cuaresma, J., Samir, K. C., Leimbach, M., Jiang, L., Kram, T., Rao, S., Emmerling, J., Ebi, K., Hasegawa, T., Havlik, P., Humpenöder, F., Da Silva, A., Smith, S., Stehfest, E., Bosetti, V., Eom, J., Gernaat, D., Masui, T., Rogelj, J., Strefler, J., Drouet, L., Krey, V., Luderer, G., Harmsen, M., Takahashi, K., Baumstark, L., Doelman, J. C., Kainuma, M., Klimont, Z., Marangoni, G., Lotze-Campen, H., Obersteiner, M., Tabeau, A., and Tavoni, M.: The Shared Socioeconomic Pathways and their energy, land use, and greenhouse gas emissions implications: An overview, Global Environ. Chang., 42, 1045 153–168, https://doi.org/10.1016/j.gloenvcha.2016.05.009, 2017.

Rodgers, C.: Inverse Methods for Atmospheric Sounding: Theory and Practice, Vol. 2 of Series on Atmospheric, Oceanic and Planetary Physics, World Scientific, Singapore, 2000.

Roy, R., Kumar, P., Kuttippurath, J., and Lefèvre, F.: Chemical ozone loss and chlorine activation in the Antarctic winters of 2013–2020, Atmos. Chem. Phys., 24, 2377–2386, https://doi.org/10.5194/acp-24-2377-2024, 2024.

928 Salawitch, R., Smith, J., Selkirk, H., Wargan, K., Chipperfield, M., Hossaini, R., Levelt, P., Livesey, N. J.,
929 McBride, L., Millan, L., Moyer, E., Santee, M. L., Schoeberl, M., Solomon, S., Stone, K., and Worden,
930 H.: The Imminent Data Desert: The Future of Stratospheric Monitoring in a Rapidly Changing
931 World, Bull. Am. Meteorol. Soc., 106, 3, E540-E563, doi:10.1175/bams-d-23-0281.1, 2025.
932 Santee, M. L., Manney, G. L., Livesey, N. J. J., Froidevaux, L., MacKenzie, I. A., Pumphrey, H. C., Read,
933 W. G., Schwartz, M. J., Waters, J. W., and Harwood, R. S.: Polar processing and development of the
934 2004 Antarctic ozone hole: first results from MLS on Aura, Geophys. Res. Lett., 32, L12817,
935 doi:10.1029/2005GL022582, 2005.
936 Santee, M. L., Manney, G. L., Livesey, N. J., Froidevaux, L., Schwartz, M. J., and Read, W. G.: Trace gas
937 evolution in the lowermost stratosphere from Aura Microwave Limb Sounder measurements, J.
938 Geophys. Res., 116, D18306, doi:10.1029/2011JD015590, 2011.
939 Santee, M. L., Manney, G. L., Lambert, A., Millán, L. F., Livesey, N. J., Pitts, M. C., Froidevaux, L., Read,
940 W. G., and Fuller, R. A.: The Influence of Stratospheric Hydration From the Hunga Eruption on
941 Chemical Processing in the 2023 Antarctic Vortex, Journal of Geophysical Research: Atmospheres, 129,
942 e2023JD040687, https://doi.org/10.1029/2023JD040687, 2024.
943 Solomon, S.: Stratospheric ozone depletion: A review of concepts and history, Rev. Geophys., 37, 275–
944 316, doi:10.1029/1999RG900008, 1999.
945 Solomon, S., D. Kinnison, J. Bandoro, and R. Garcia, Simulation of polar ozone depletion: An update, J.
946 Geophys. Res. Atmos., 120, 7958–7974, doi:10.1002/2015JD023365, 2015.
947 Solomon, S., Ivy, D. J., Kinnison, D., Nills, M. J., Neely, R. R., and Schmidt, A.: Emergence of healing in
948 the Antarctic ozone layer, Science, 353 (6296), 269-274, doi:10.1126/science.aae0061, 2016.
949 Strahan, S. E., Douglass, A. R., Newman, P. A., and Steenrod, S. D.: Inorganic chlorine variability in the
950 Antarctic vortex and implications for ozone recovery, J. Geophys. Res. Atmos., 119, 14,098–14,109,
951 https://doi.org/10.1002/2014JD022295, 2014.
952 Strahan, S. E., and Douglass, A. R.: Decline in Antarctic ozone depletion and lower stratospheric chlorine
953 determined from Aura Microwave Limb Sounder observations. Geophys. Res. Lett., 45, 382–390,
954 https://doi.org/10.1002/2017GL074830, 2018.
955 Strahan, S. E., Douglass, A. R., and Damon, M. R.: Why do Antarctic ozone recovery trends vary?, J.
956 Geophys. Res.-Atmos., 124, 8837–8850, https://doi.org/10.1029/2019JD030996, 2019.
957 Strahan, S. E., Smale, D., Douglass, A. R., Blumenstock, T., Hannigan, J. W., Hase, F., Jones, N. B.,
958 Mahieu, E., Notholt, J., Oman, L. D., Ortega, I., Palm, M., Prignon, M., Robinson, J., Schneider, M.,
959 Sussmann, R., and Velazco, V. A.: Observed hemispheric asymmetry in stratospheric transport trends
960 from 1994 to 2018, Geophys. Res. Lett., 47, e2020GL088567, https://doi. org/10.1029/2020GL088567,
961 2020.

962 Tilmes, S., Muller, R., Grooß, J.-U., and Russell, J. M.: Ozone loss and chlorine activation in the Arctic
963 winters 1991–2003 derived with the tracer-tracer correlations, Atmos. Chem. Phys., 4, 2181–2213,
964 http://www.atmos-chem-phys.net/4/2181/2004/, 2004.
965 von der Gathen, P., Rex, M., Harris, N. R. P., Lucic, D., Knudsen, B. M., Braathen, G. O., de Backer, H.,
966 Fabian, R., Fast, H., Gil, M., Kyrö, E., Mikkelsen, I. S., Rummukainen, M., Stähelin, J., and Varotsos,
967 C.: Observational evidence for chemical ozone depletion over the Arctic in winter 1991–92, Nature,
968 375, 131–134, 1995.
969 Wang, P., Solomon, S., Santer, B. D., Kinnison, D. E., Fu, Q., Stone, K. A., Zhang, J., Manney, G. L., and
970 Millan, L. F.: Fingerprinting the recovery of Antarctic ozone, Nature, 649, 646–651,
971 https://doi.org/10.1038/s41586-025-08640-9, 2025.
972 Wargan, K., Weir, B., Manney, G. L., Cohn, S., and Livesey, N. J.: The anomalous 2019 Antarctic ozone
973 hole in the GEOS Constituent Data Assimilation System with MLS observations, J. Geophys. Res.-
974 Atmos., 125, e2020JD033335, https://doi.org/10.1029/2020JD033335, 2020.
975 Waters, J., Froidevaux, L., Harwood, R., Jarnot, R., Pickett, H., Read, W., Siegel, P., Cofield, R., Filipiak,
976 M., Flower, D., Holden, J., Lau, G., Livesey, N., Manney, G., Pumphrey, H., Santee, M., Wu, D., Cuddy,
977 D., Lay, R., Loo, M., Perun, V., Schwartz, M., Stek, P., Thurstans, R., Boyles, M., Chandra, S., Chavez,
978 M., Chen, G.-S., Chudasama, B., Dodge, R., Fuller, R., Girard, M., Jiang, J., Jiang, Y., Knosp, B.,
979 LaBelle, R., Lam, J., Lee, K., Miller, D., Oswald, J., Patel, N., Pukala, D., Quintero, O., Scaff, D.,
980 Snyder, V., Tope, M., Wagner, P., and Walch, M.: The Earth Observing System Microwave Limb
981 Sounder (EOS MLS) on the Aura satellite, IEEE Transac. Geosci. Remote Sens., 44, 5,
982 https://doi.org/10.1109/TGRS.2006.873771, 2006.
983 Weber, M., Coldewey-Egbers, M., Fioletov, V. E., Frith, S. M., Wild, J. D., Burrows, J. P., Long, C. S.,
984 and Loyola, D.: Total ozone trends from 1979 to 2016 derived from five merged observational datasets
985 – the emergence into ozone recovery, Atmos. Chem. Phys., 18, 2097–2117, https://doi.org/10.5194/acp-
986 18-2097-2018, 2018.
987 Wegner, T., Kinnison, D. E., Garcia, R. R., and Solomon, S.: Simulation of polar stratospheric clouds in
988 the specified dynamics version of the whole atmosphere community climate model, J. Geophys. Res.-
989 Atmos., 118, 4991–5002, https://doi.org/10.1002/jgrd.50415, 2013.
990 Weimer, M., Kinnison, D. E., Wilka, C., and Solomon, S.: Effects of denitrification on the distributions of
991 trace gas abundances in the polar regions: a comparison of WACCM with observations, Atmos. Chem.
992 Phys., 23, https://doi.org/10.5194/acp-23-6849-2023, 2023.
993 Wilka, C., Solomon, S., Kinnison, D., and Tarasick, D.: An Arctic ozone hole in 2020 if not for the Montreal
994 Protocol, https://doi.org/10.5194/acp-21-15771-2021, 2021.

WMO: Scientific Assessment of Ozone Depletion: 2018, Global Ozone Research and Monitoring Project–Report No. 58, 588 pp., WMO, Geneva, Switzerland, ISBN: 978-1-7329317-1- 8, 2018.

WMO: Scientific Assessment of Ozone Depletion: 2022, GAW Report No. 278, 509 pp., WMO, Geneva, Switzerland, ISBN: 978-9914-733-97-6, 2022.

Zhang, Z.-Y., Gong, D.-Y., He, X.-Z., Lei, Y.-N., and Feng, S.-H.: Statistical reconstruction of the Antarctic Oscillation Index based on multiple proxies, Atmos. Ocean. Sci. Lett., 3, 5, 283-287, https://doi.org/10.1080/16742834.2010.11446883, 2010.

Ziemke, J. R., Oman, L. D., Strode, S. A., Douglass, A. R., Olsen, M. A., McPeters, R. D., Bhartia, P. K., Froidevaux, L., Labow, G. J., Witte, J. C., Thompson, A. M., Haffner, D. P., Kramarova, N. A., Frith, S. M., Huang, L.-K., Jaross, G. R., Seftor, C. J., Deland, M. T., and Taylor, S. L.: Trends in global tropospheric ozone inferred from a composite record of TOMS/OMI/MLS/OMPS satellite measurements and the MERRA-2 GMI simulation, Atmos. Chem. Phys., 19, 3257–3269, https://doi.org/10.5194/acp-19-3257-2019, 2019.

Figures

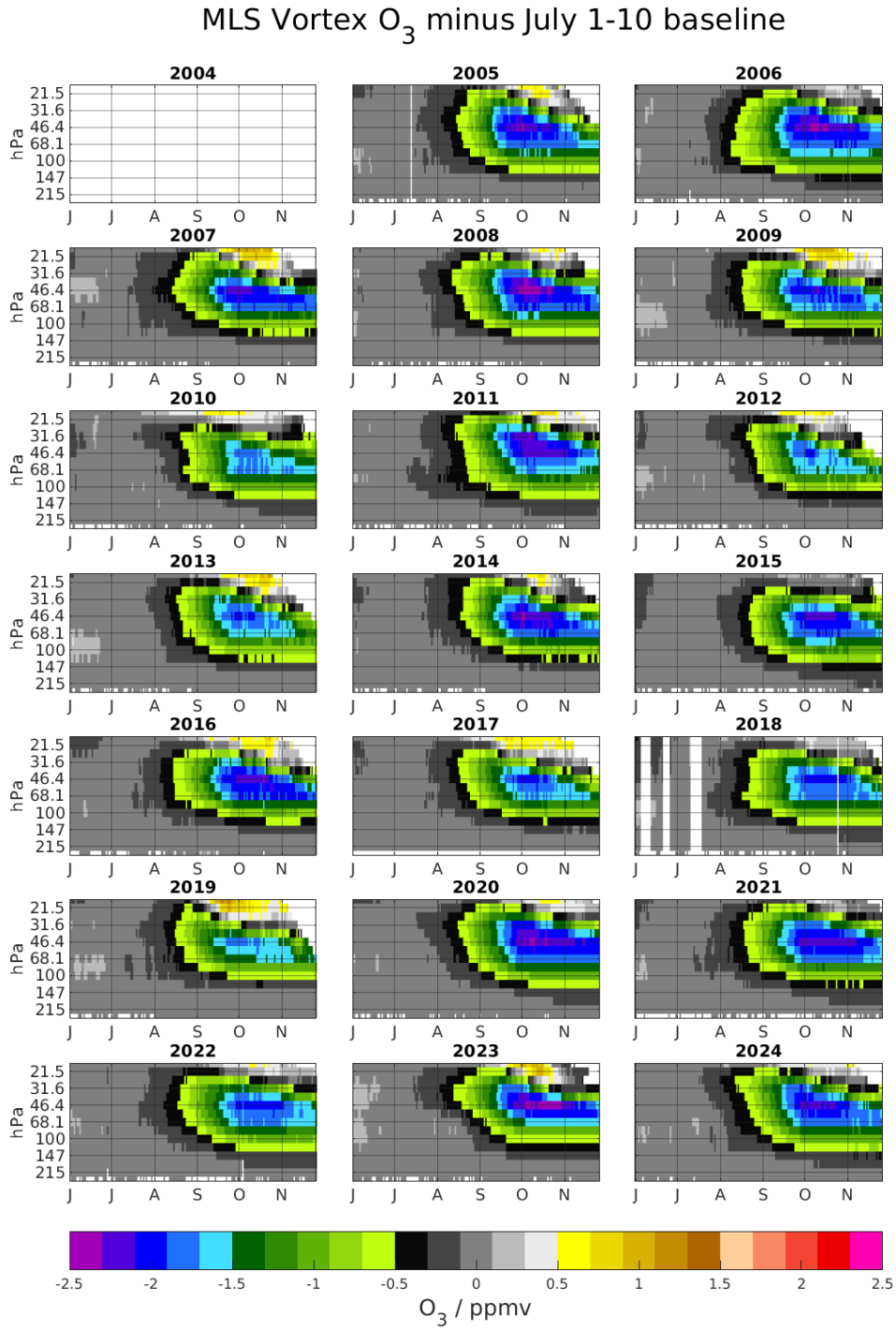

Figure 1. June to November vortex-average lower stratospheric ozone profiles over the range 215–21 hPa for 2005-2024. The respective July 1-10 average is subtracted for each year to remove interannual variability of early-winter (baseline) conditions. Partial 2004 is not included because MLS operations had not begun in July, so this baseline could not be calculated

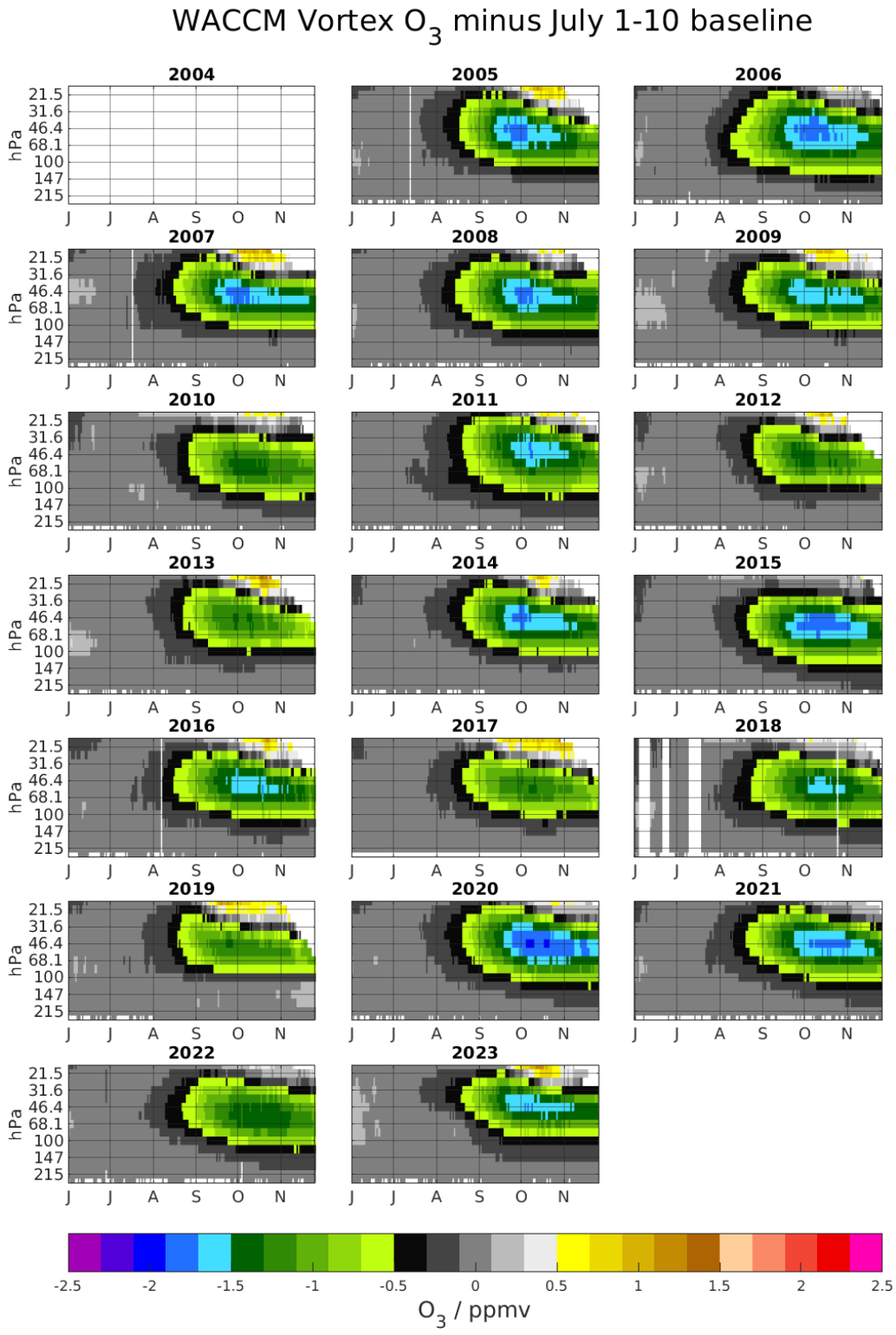

Figure 2. Same as Fig. 1, but for the WACCM simulation and without year 2024.

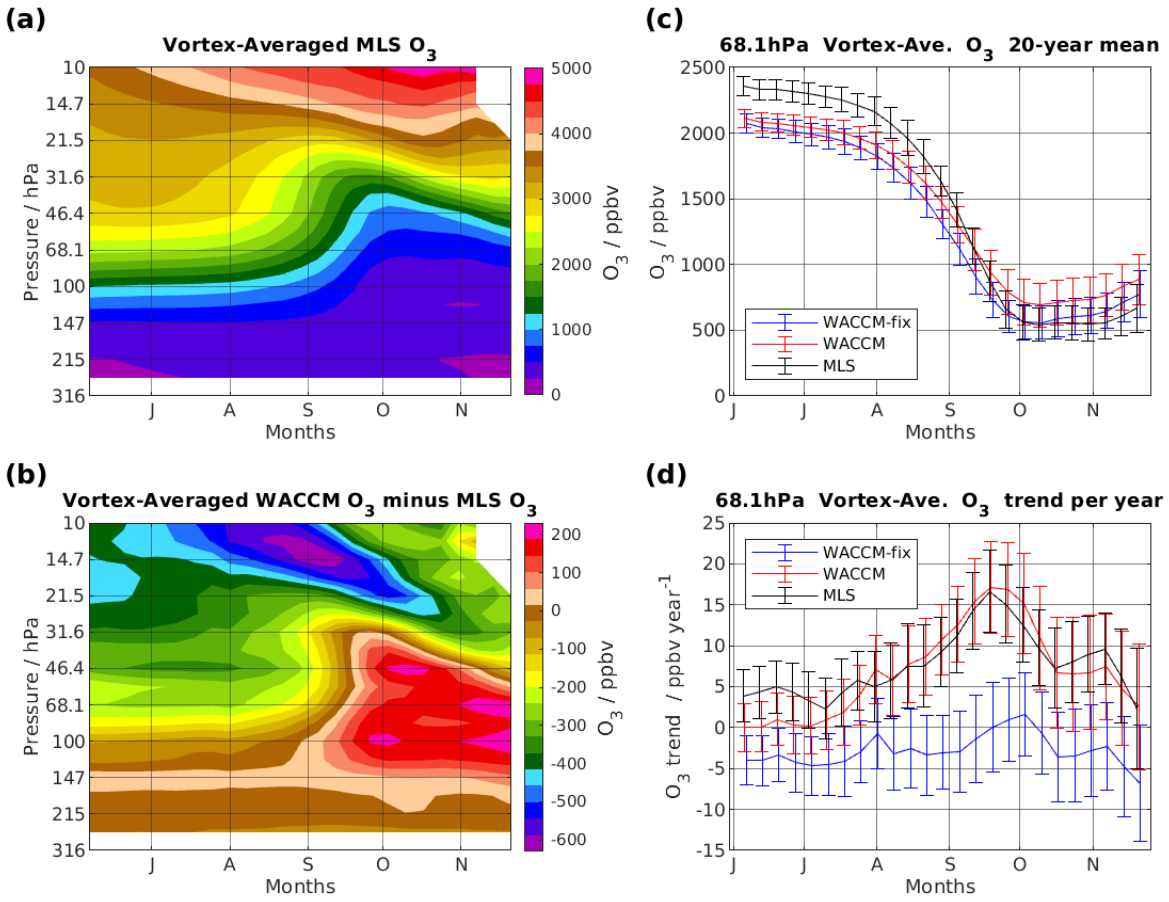

Figure 3. (a) Weekly mean Antarctic vortex-average ozone values from MLS in the lower stratosphere from early June to late November (weeks centered on day of year 157–325) for 2004 through 2023. (b) Average values from WACCM, as in (a), minus the MLS values shown in (a). (c) Example at 68 hPa of the mean ozone abundances for 2004–2023 from MLS, WACCM, and WACCM-fix-EESC (labelled "WACCM-fix"); the error bars represent the interannual standard deviation about the mean in these weekly average values over all the years. (d) Ozone trends (ppbv yr^{-1}) at 68 hPa obtained by fitting a simple linear trend to the yearly O_3 values contributing to each weekly average. Weeks prior to the start of MLS science data collection on July 28, 2004 are not included in these averages; thus results for the first eight weeks are 19-yr averages and trends.

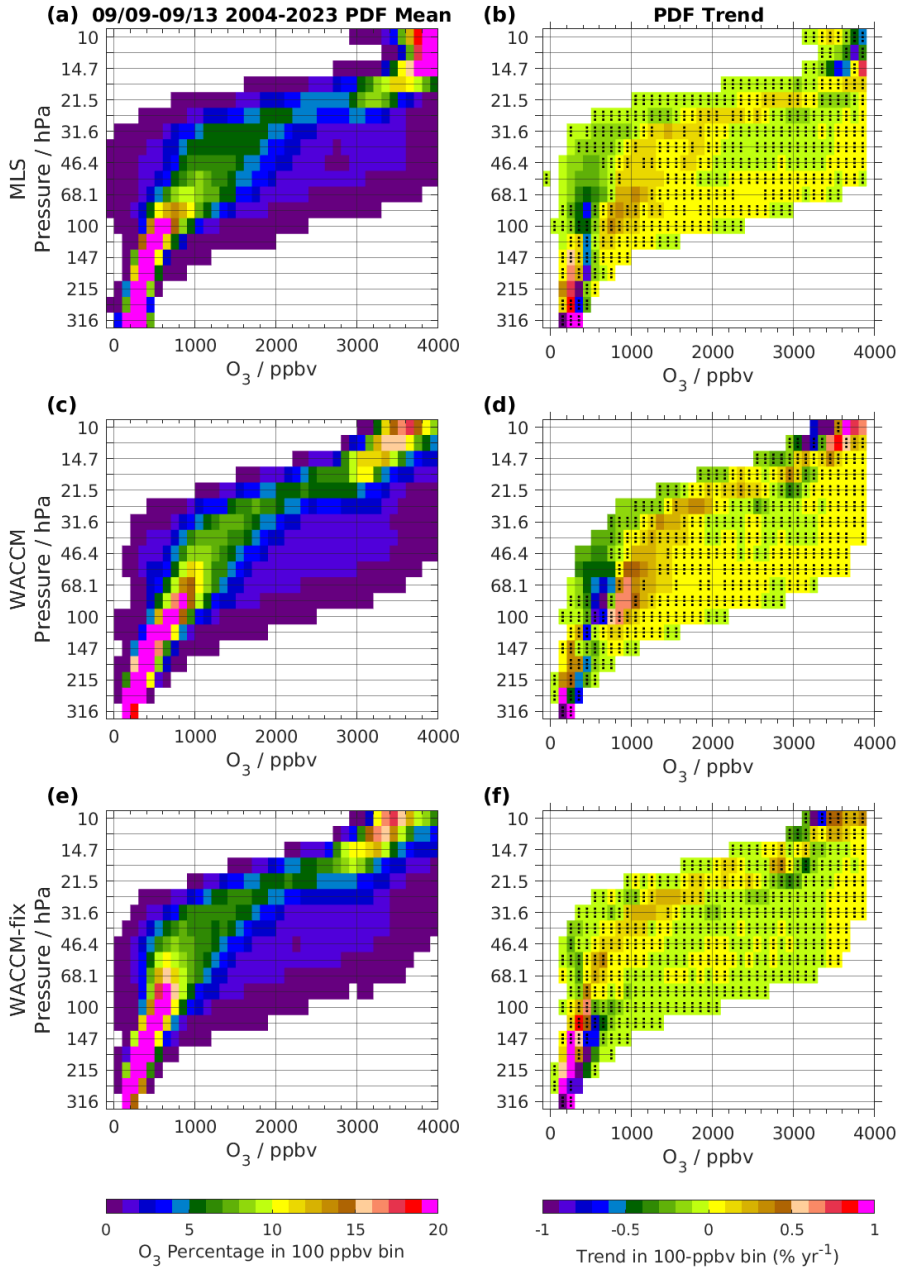

Figure 4. (a) A histogram of all MLS lower-stratospheric vortex O_3 observations from the week of September 9–15 for 2004–2023, normalized separately for each level, representing the underlying PDF. (b) PDF (histogram) trends shown are the slopes from linear fits within each bin to values from histograms prepared as in (a), but separately for each year. Bins without black stippling have trends that are larger in magnitude than the 1σ uncertainty in the trend. (c) and (d) are the same as (a) and (b), respectively, but for the WACCM simulation. (e) and (f) are the same as (a) and (b), respectively, but for the WACCM-fix-EESC simulation.

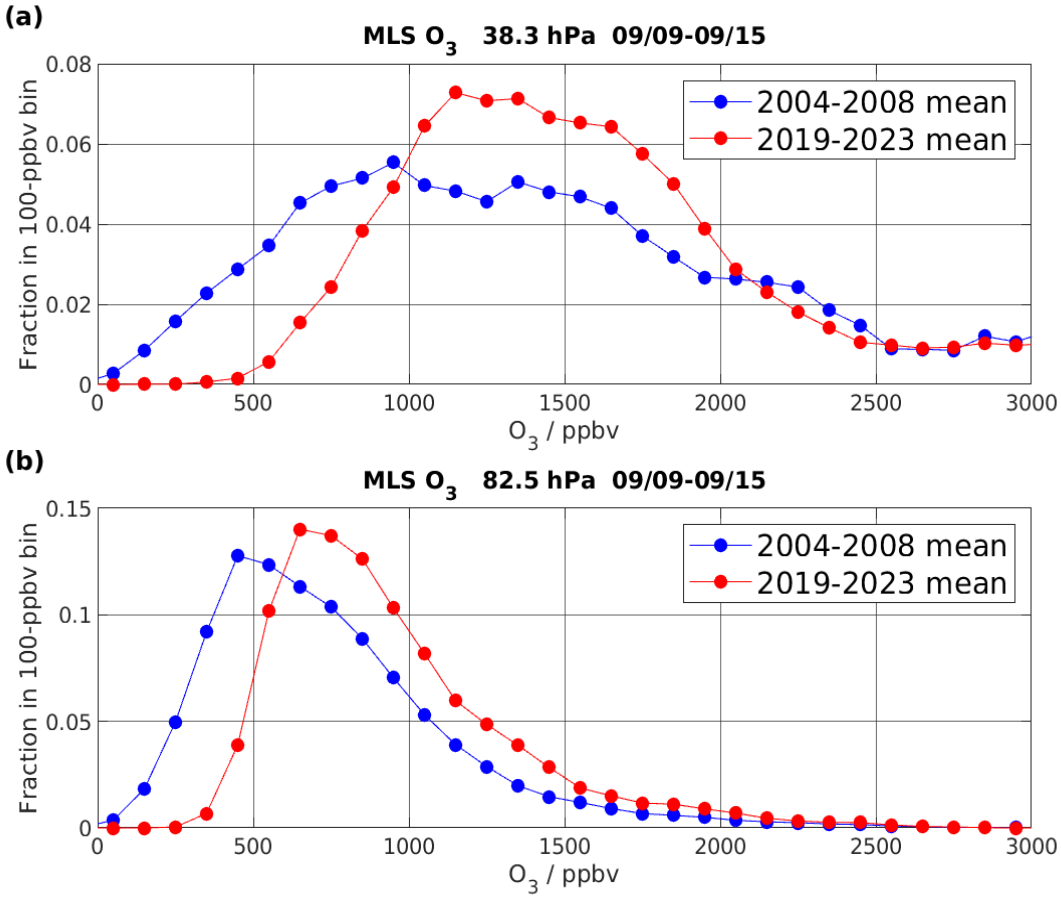

Figure 5. Fraction of the Antarctic vortex-average MLS ozone distributions in each 100 ppbv bin, for the week centered on September 12 for the periods 2004–2008 (blue) and 2019–2023 (red), at (a) 38.3 hPa and (b) 82.5 hPa.

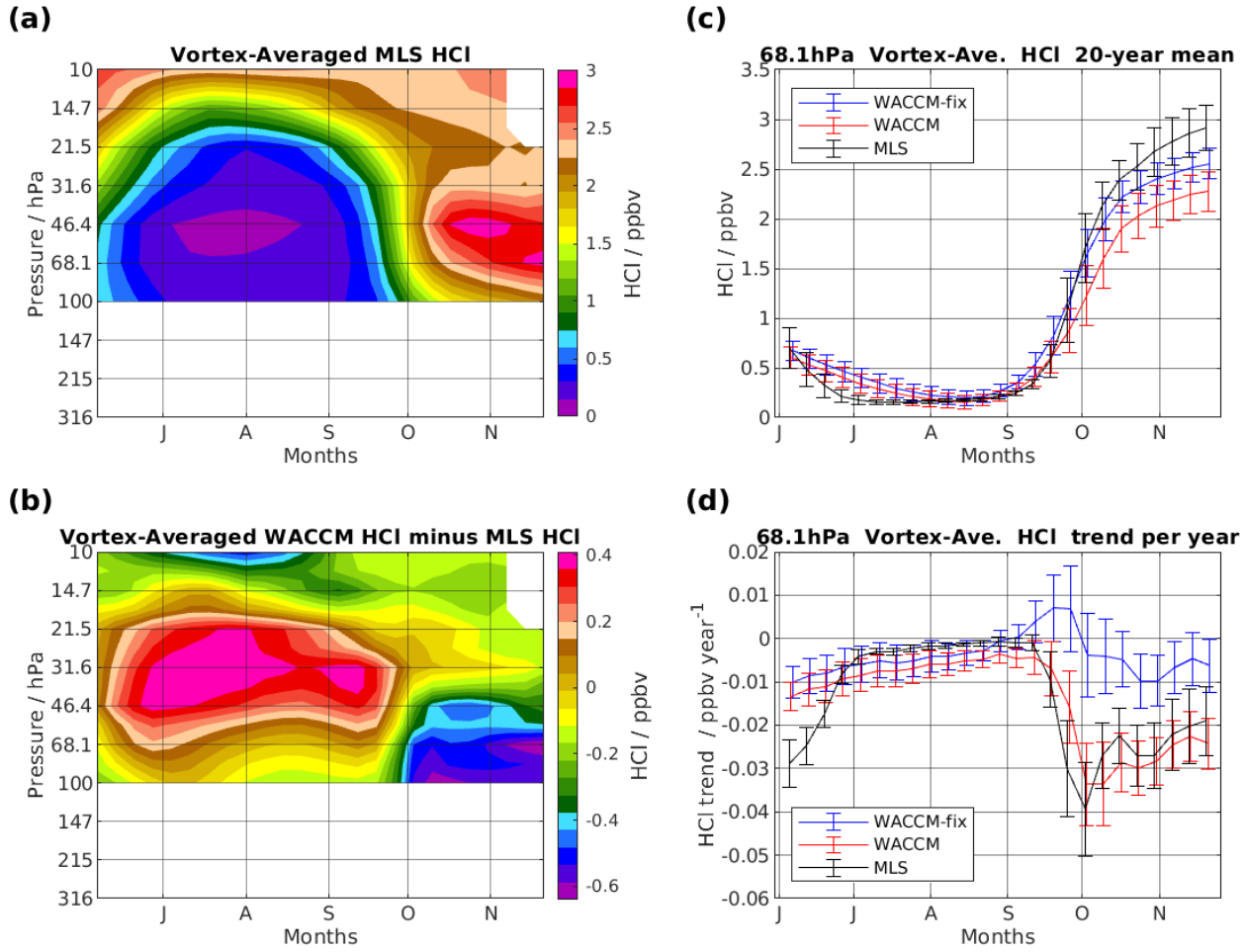

Figure 6. Same as Fig. 3, but for HCl.

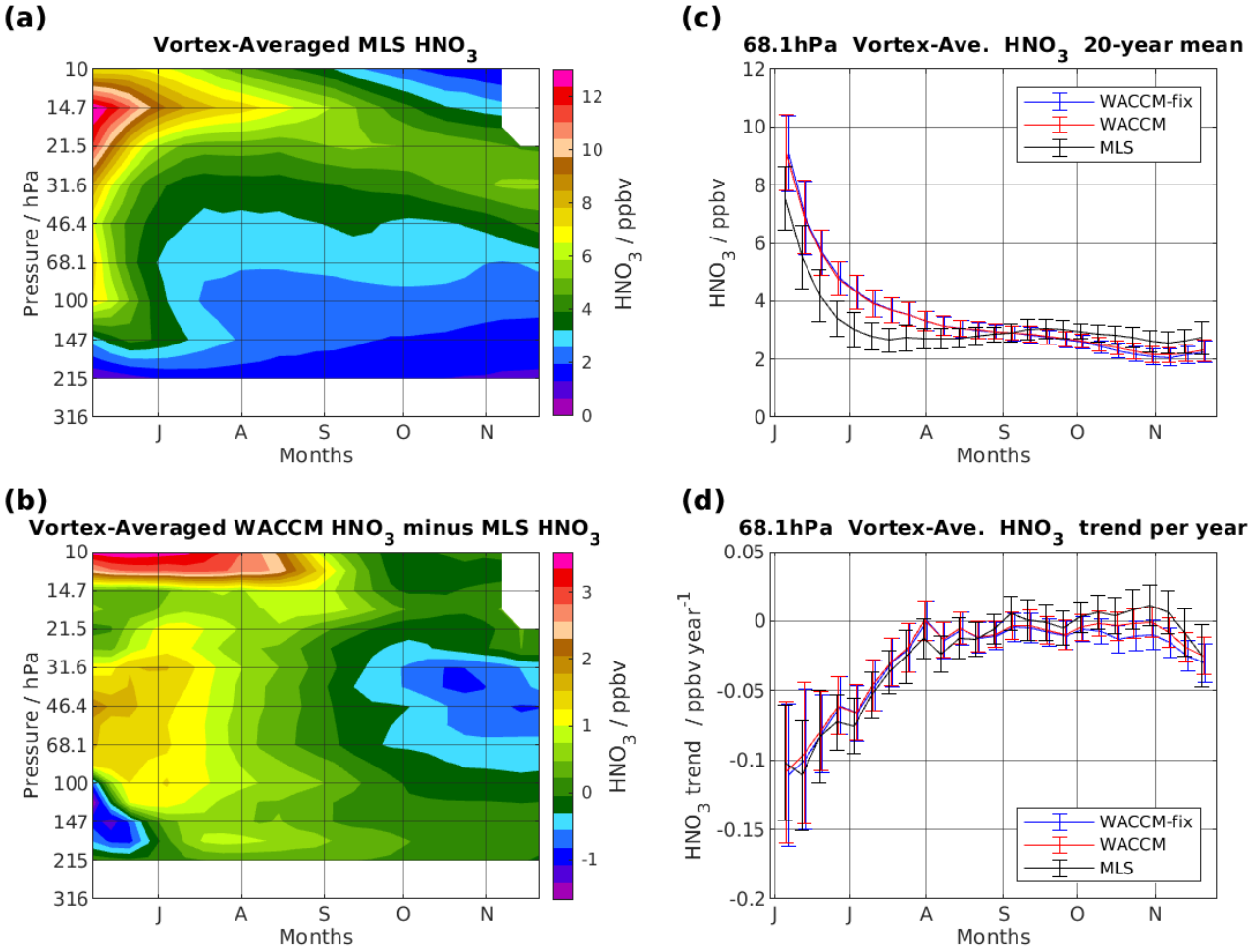

Figure 7. Same as Fig. 3, but for HNO_3.

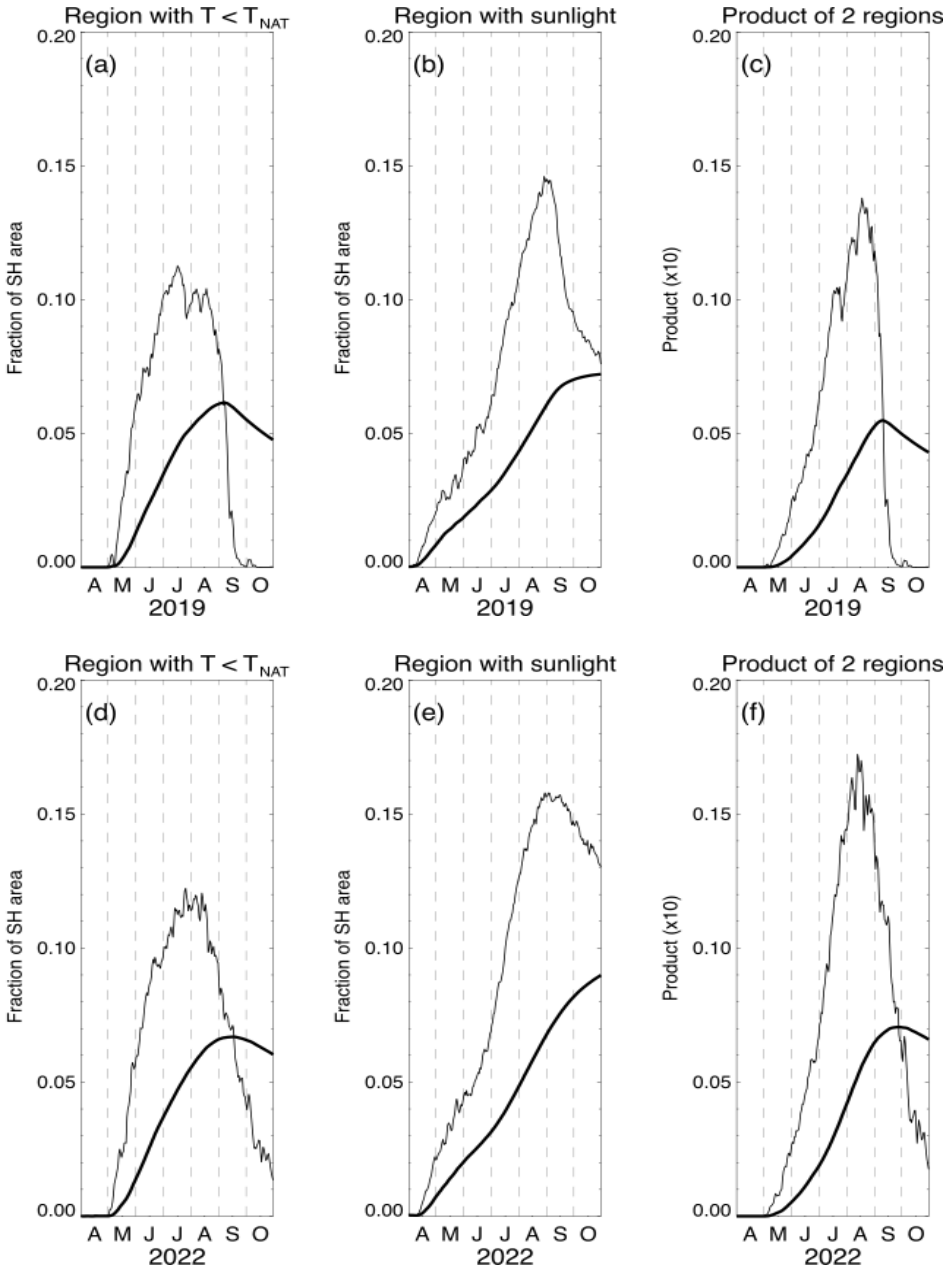

Figure 8. The lower stratospheric layer-average Antarctic vortex area with $T < T_{NAT}$ for (a) 2019 and (d) 2022; the lower stratospheric layer-average Antarctic vortex area exposed to sunlight for (b) 2019 and (e) 2022; and the product (multiplied by 10) of these two layer-average areas for (c) 2019 and (f) 2022. Layer averages are calculated over potential temperature levels from 330 K to 620 K. The thin lines depict daily quantities, whereas the thick lines are time-averaged values of these quantities through each day of the year, from April 1. The layer-average area diagnostics are expressed as a fraction of the total Southern Hemisphere (SH) area.

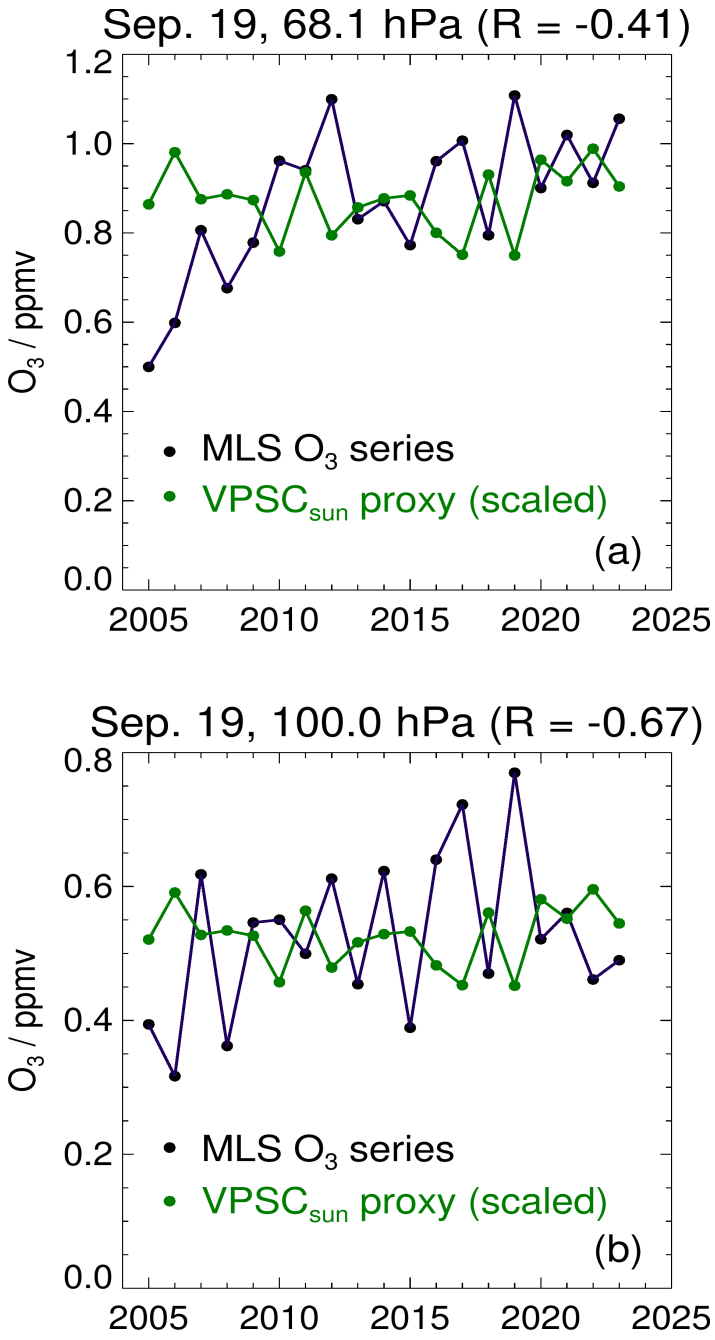

Figure 9. Vortex-average Antarctic ozone variations from MLS (black) over 2005–2023 for the week centered on September 19 at (a) 68 hPa and (b) 100 hPa. The green lines are a scaled version of the variability in the *VPSC*$_{sun}$ proxy term described in the text (in relation to Fig. 8); the scaling (using the average ozone value over the years divided by the average relative change in the proxy) is applied here to show the relative changes in this proxy from year to year on the same scale as the ozone ranges in each panel.

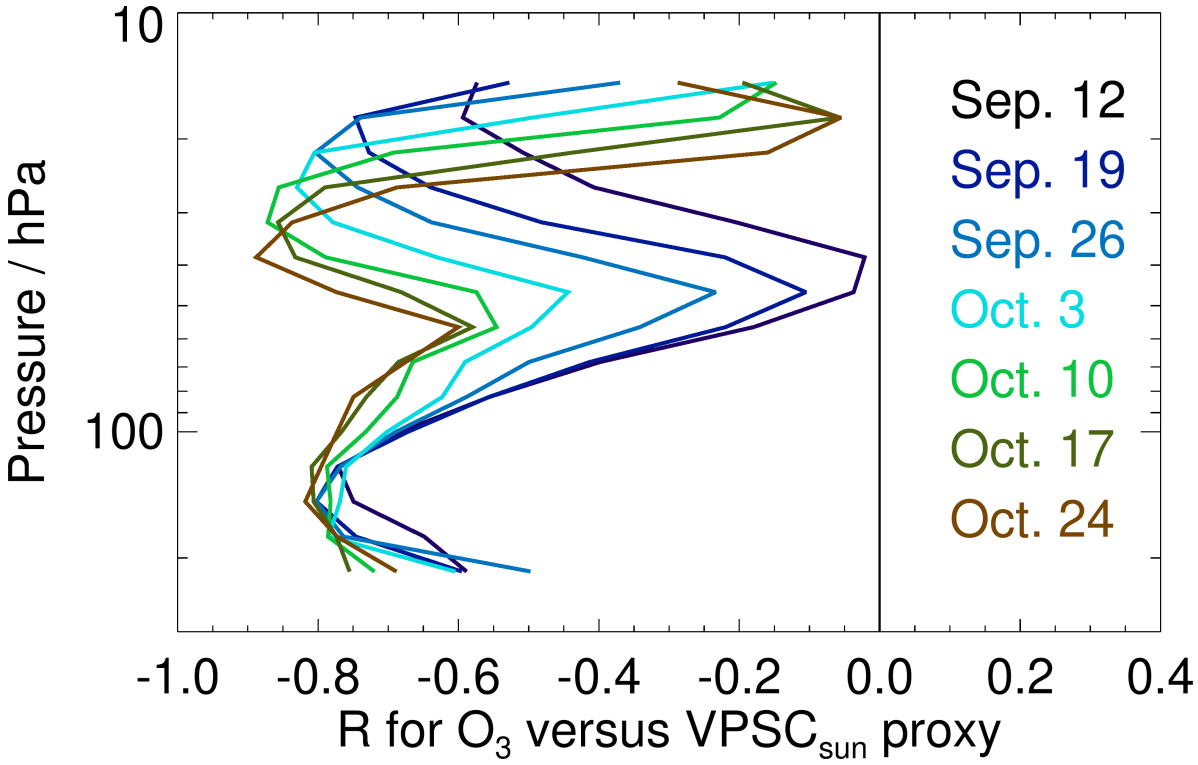

Figure 10. An expanded view of the correlation coefficient (R) between the ozone vortex-average time series and the lower stratospheric $VPSC_{sun}$ proxy described in the text and in Fig. 8. Results are shown as a function of pressure for each of the September and October weeks considered here, as labeled on the right side of this plot.

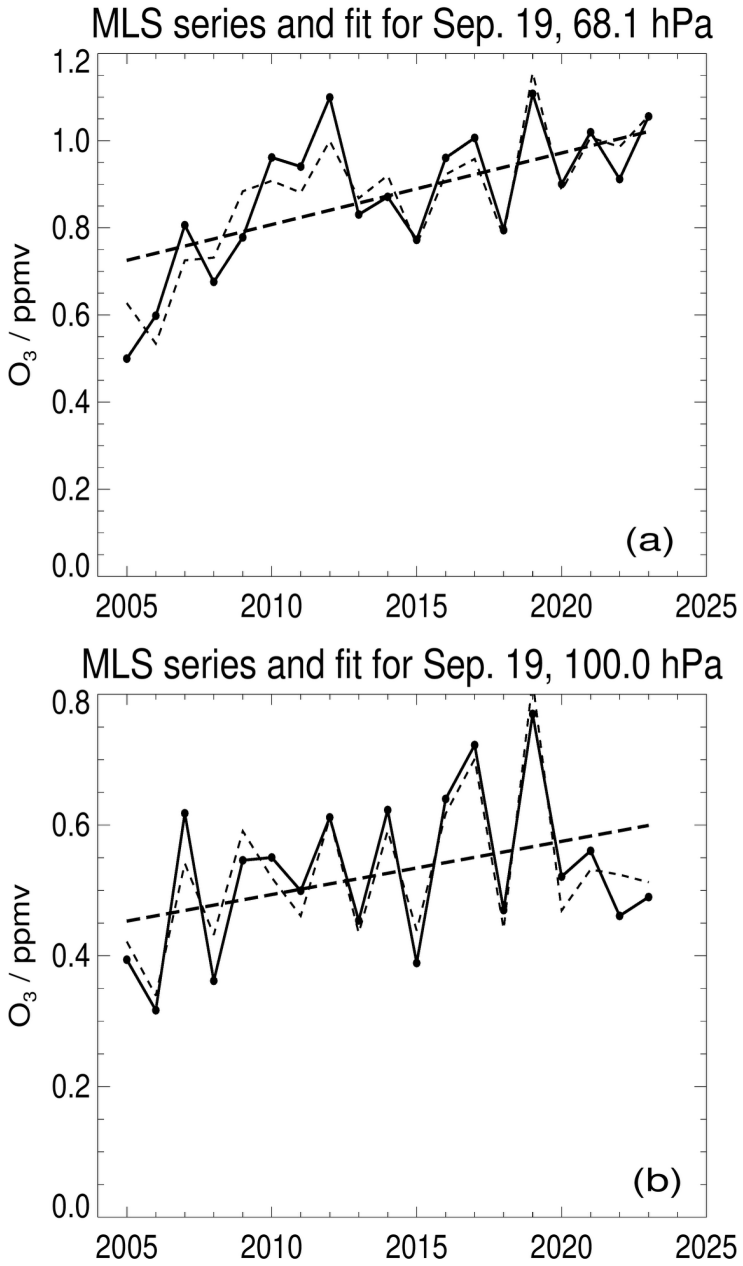

Figure 11. Examples of MLR fits to the MLS vortex-average ozone time series at (a) 68 hPa and (b) 100 hPa for the week centered on September 19. The MLS ozone averages are given by the solid line, the ozone trend (slope component of the MLR fit) is shown by the thick dashed line, and the thin dashed line gives the full fit from the MLR analysis.

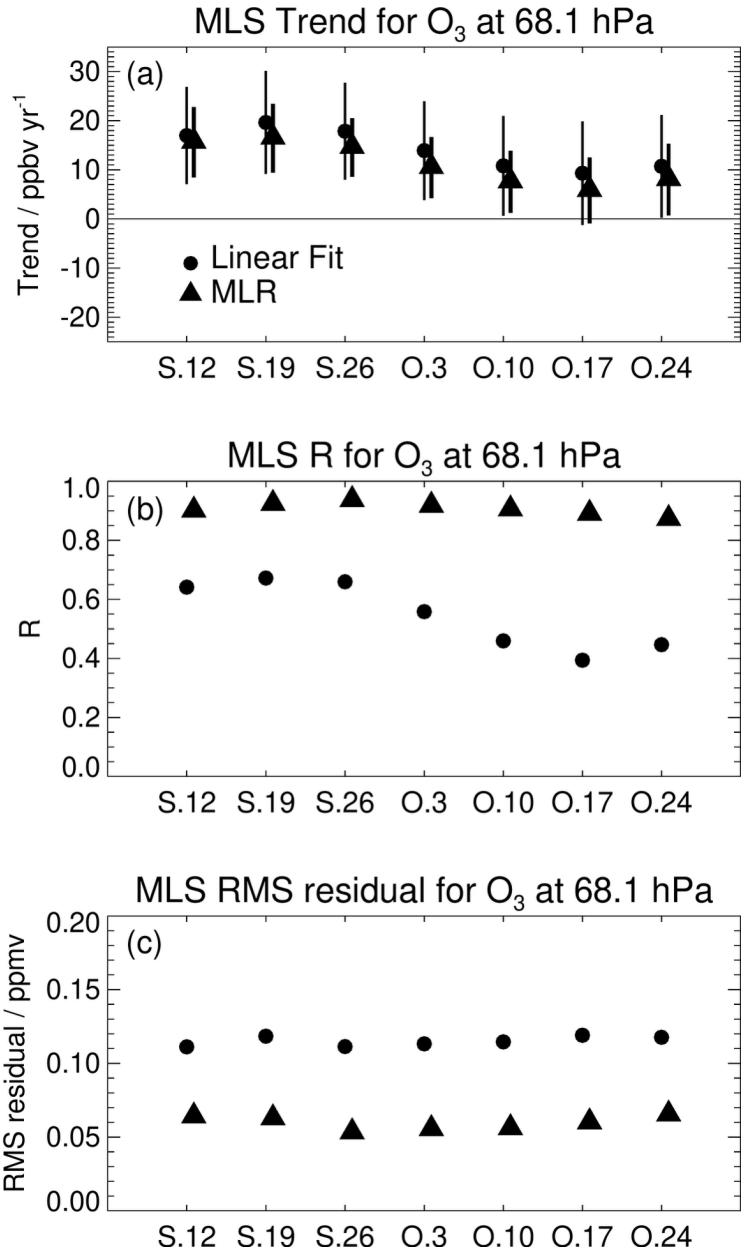

Figure 12. Results at 68 hPa for (a) the trends in MLS vortex-average ozone over Antarctica, (b) the correlation coefficients between the fits and the MLS O_3 series and (c) the RMS residuals for these fits, as a function of weeks in September and October (centered on September 12, labeled S.12, to October 24, labeled O.24). The filled circles and filled triangles represent results from a simple linear fit and MLR, respectively, for 2005–2023. Trend error bars in (a) represent 2σ.

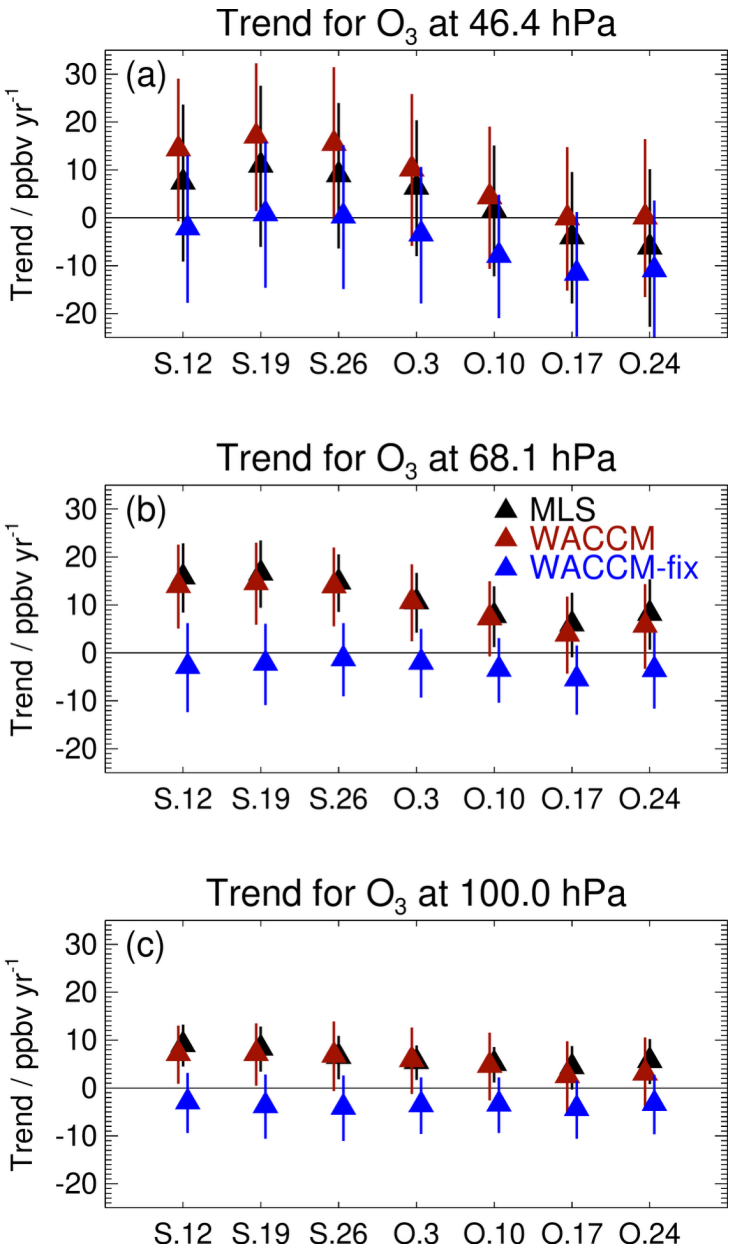

Figure 13. A comparison of the vortex-average trends for 2005–2023 based on MLR analyses from MLS, WACCM, and WACCM-fix-EESC (labeled WACCM-fix) for the weeks from September 12 through October 24 for (a) 46 hPa, (b) 68 hPa, and (c) 100 hPa.

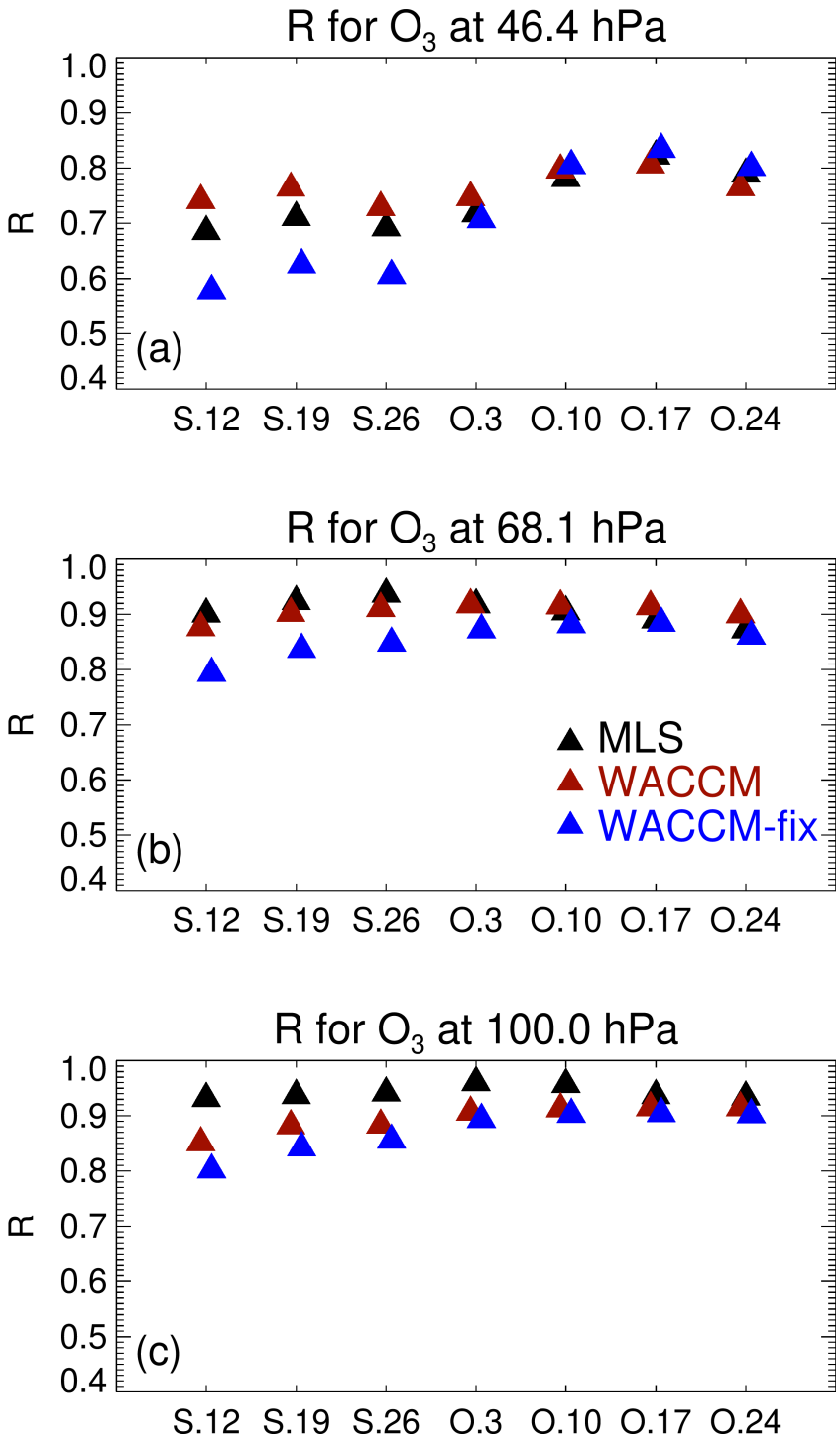

Figure 14. Same as Fig. 13, but for the correlation coefficients (R) calculated for the MLR fits to the vortex-average ozone time series.

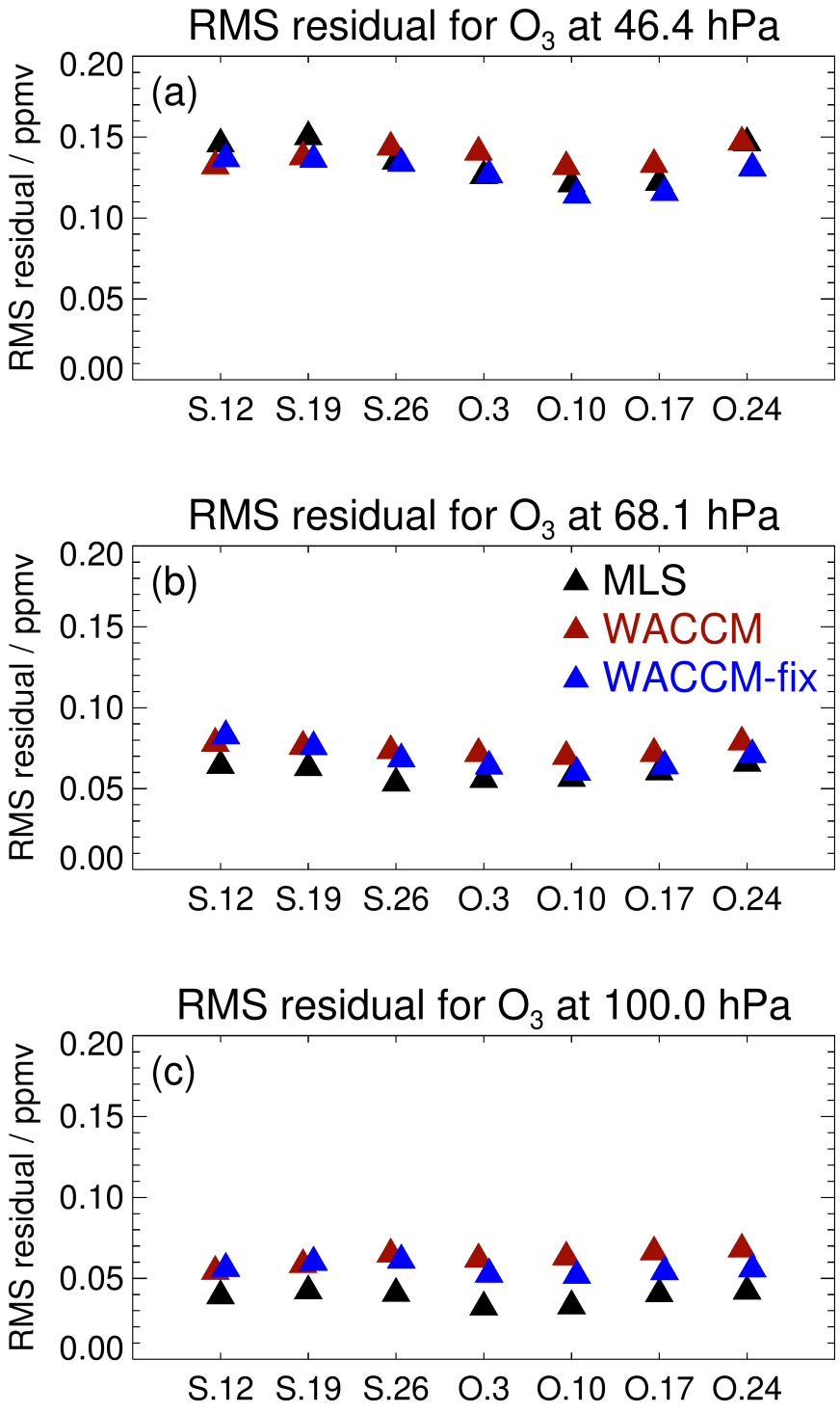

Figure 15. Same as Fig. 13, but for the RMS residuals of the MLR fits to the vortex-average ozone time series.

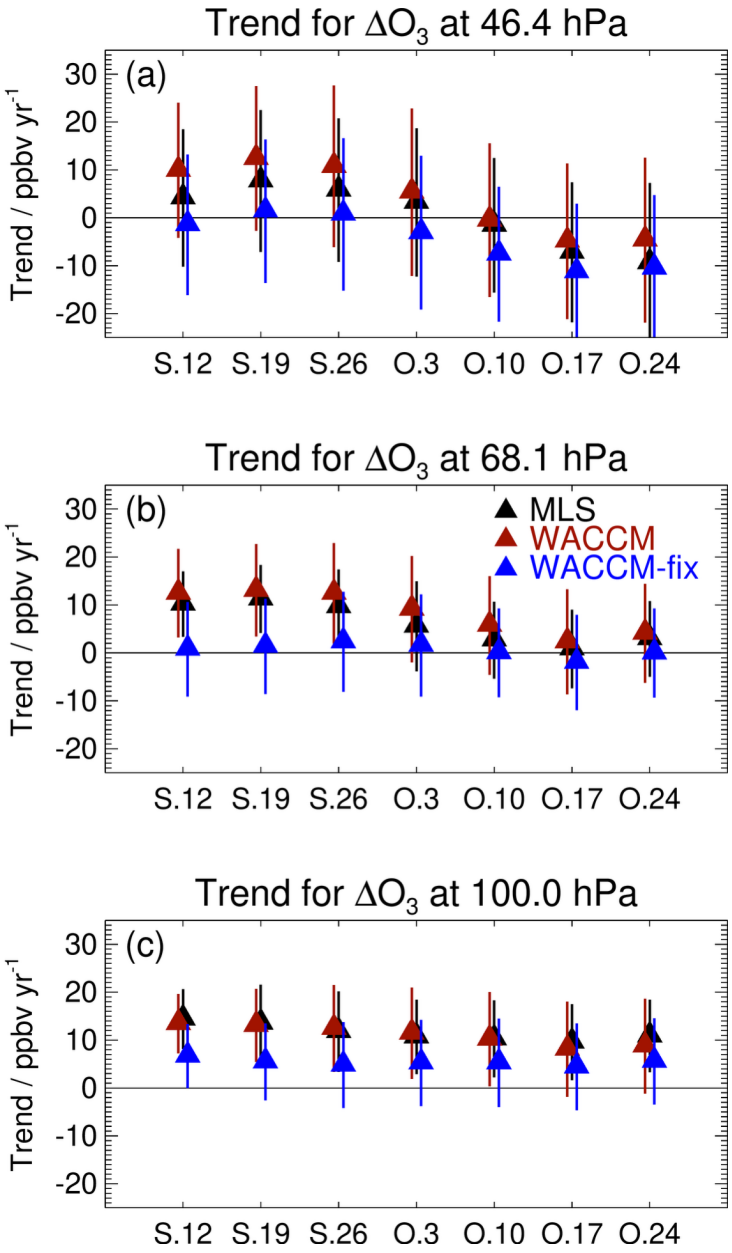

Figure 16. Same as Fig. 13, but for MLR analysis results from time series of vortex-average ozone in the first week of July subtracted from the September and October weekly average ozone values; we refer to this methodology as ΔO_3 analyses rather than O_3 analyses.

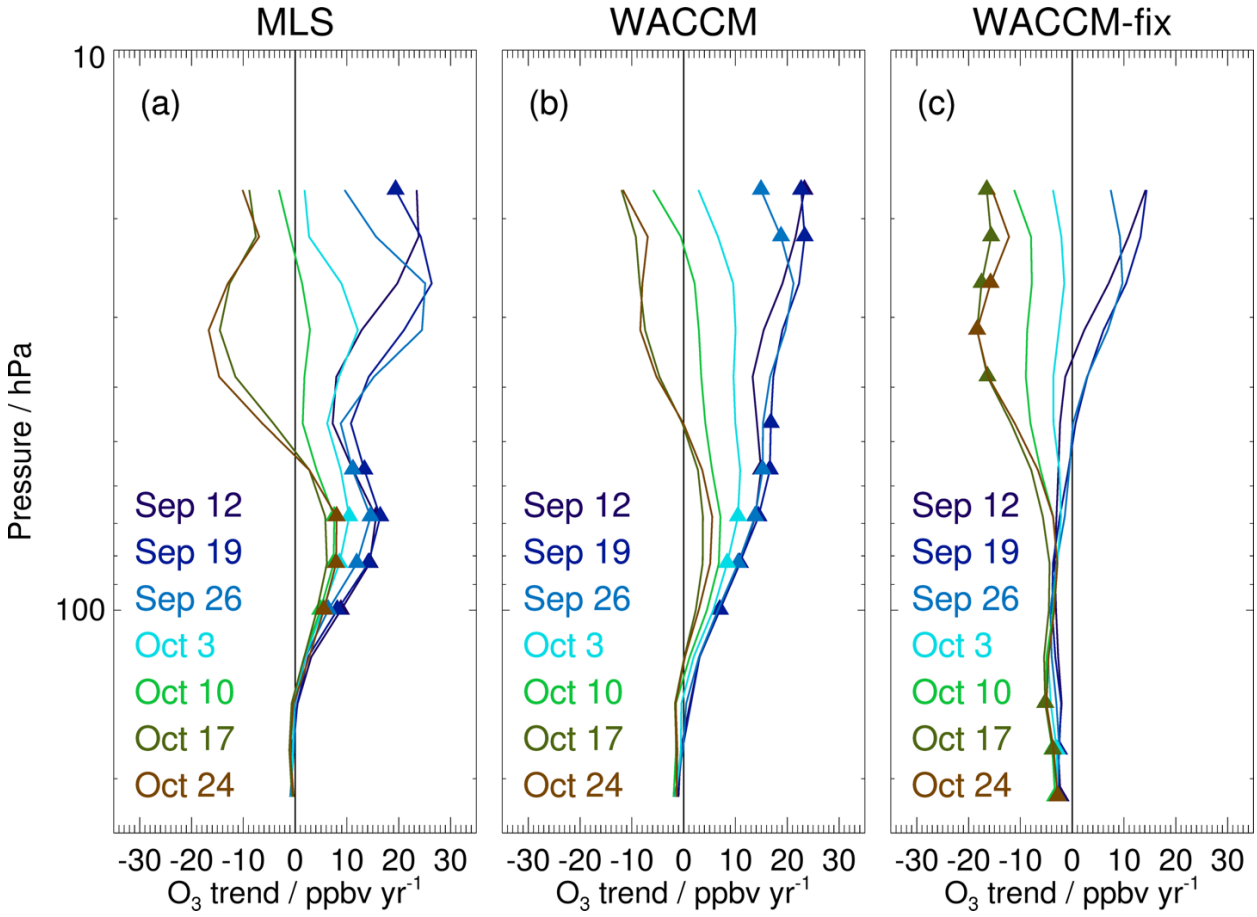

Figure 17. Trends in Antarctic vortex-average ozone from (a) MLS, (b) WACCM, and (c) WACCM-fix-EESC (labeled WACCM-fix) based on MLR analyses from 2005 to 2023. The different curves depict weekly averages centered on the dates shown. The trends that exhibit statistical significance (based on our definition at the 2σ level) are marked by triangles.

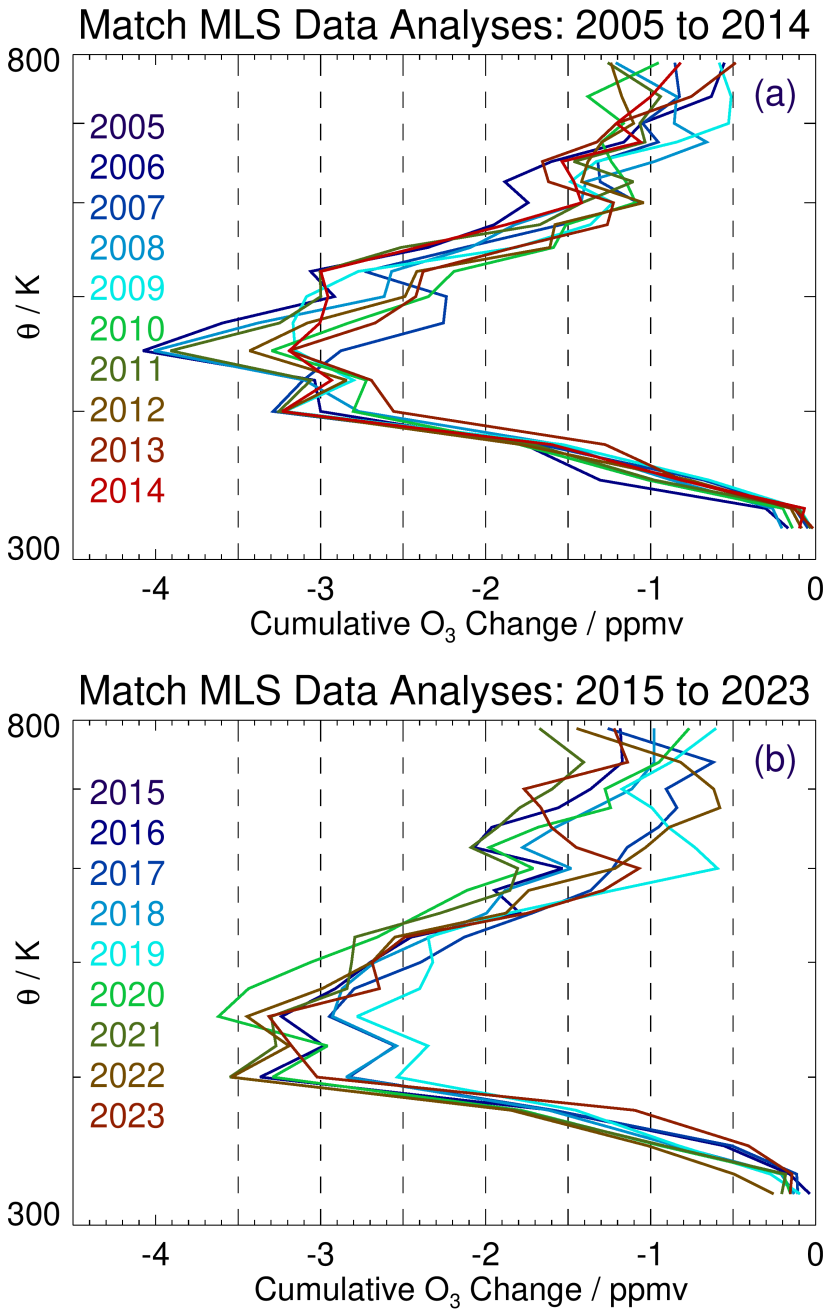

Figure 18. Profiles of maximum cumulative ozone change (with a negative value representing a loss) from the Match technique inside the Antarctic vortex, based on weekly averages in the winter/spring for (a) 2005–2014 and (b) 2015–2023.

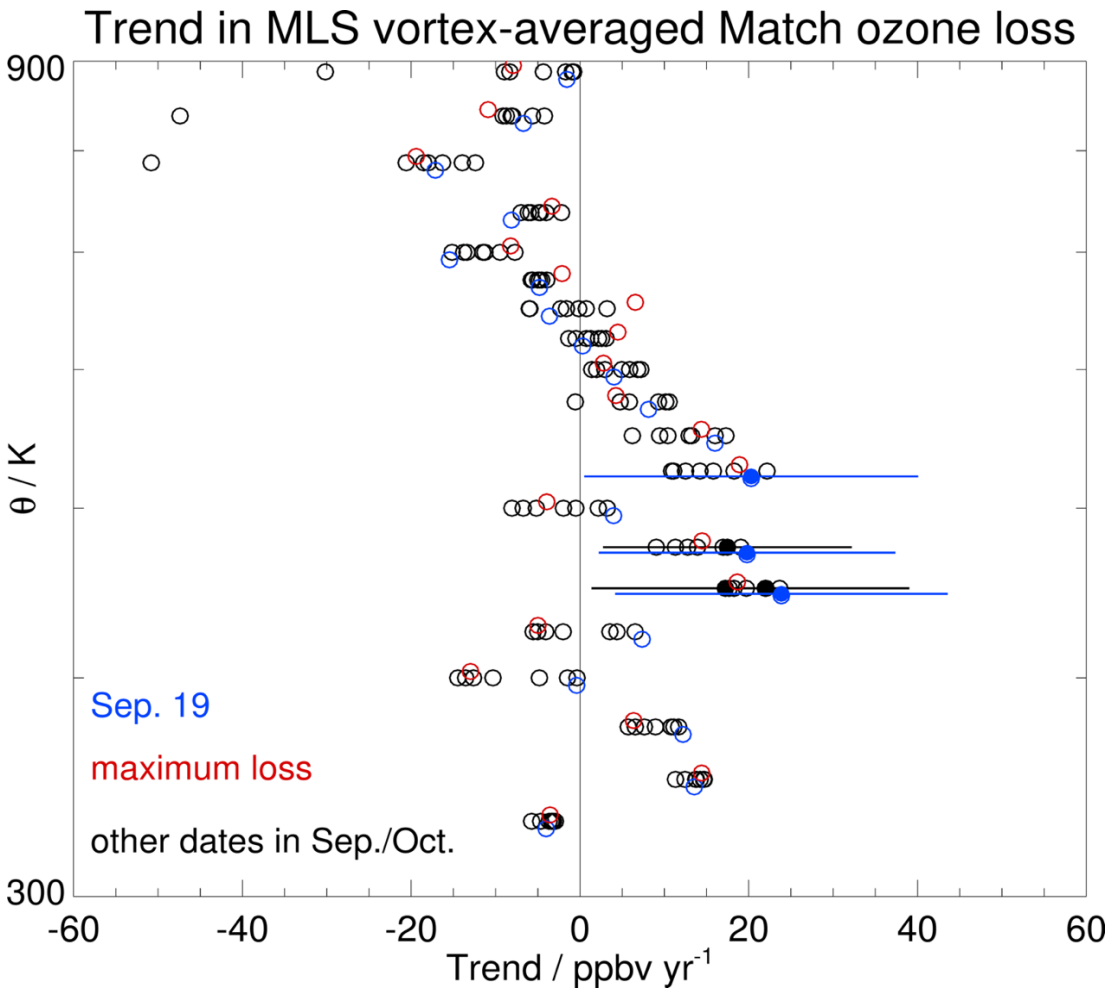

Figure 19. Chemical ozone loss trend profiles inside the Antarctic lower stratospheric vortex from Match-based analyses of MLS data from May through October, for 2005–2023. Only a few trends, marked by the filled circles with associated (2σ) error bars, are significant; for clarity, other error bars are omitted. The blue circles are for the week centered on September 19, the red circles are trends based on the maximum cumulative losses for each year, and the other points (in black) represent trend values for the other analyzed weeks, from September 12 to October 24.

Supplement

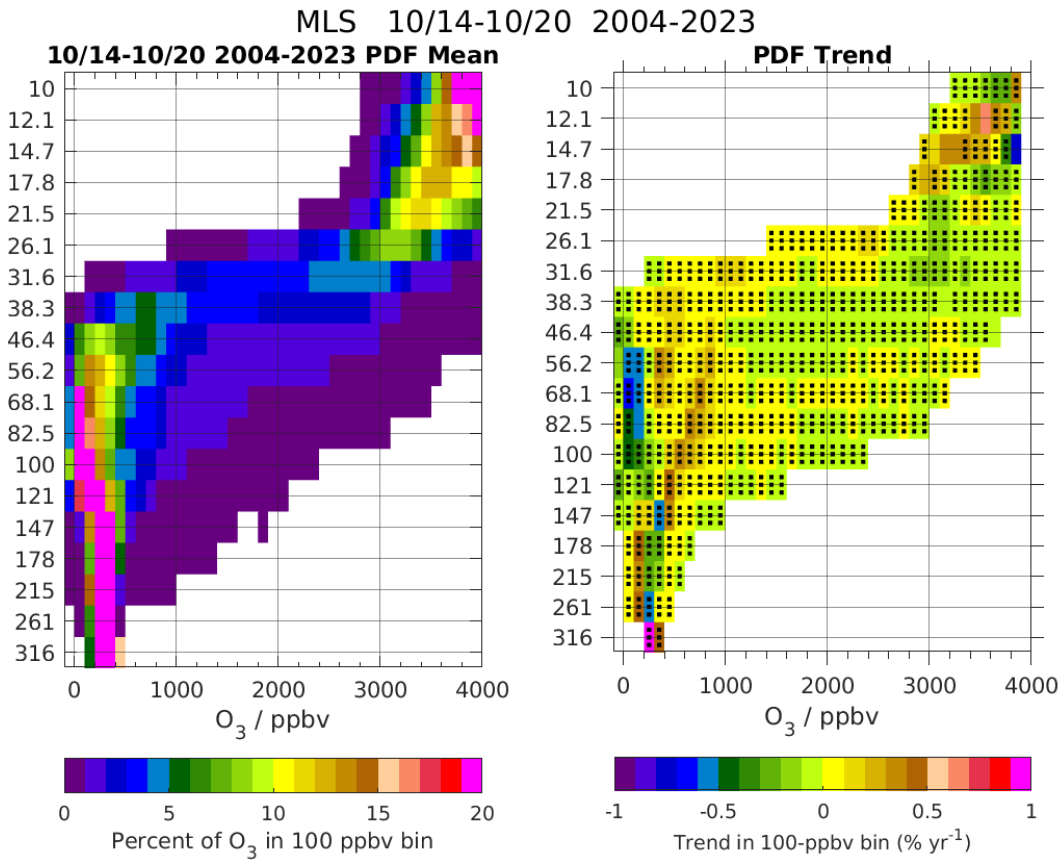

Figure S1. Same as the MLS-related panels in Fig. 4 in the main text, but for the week of October 14–20.

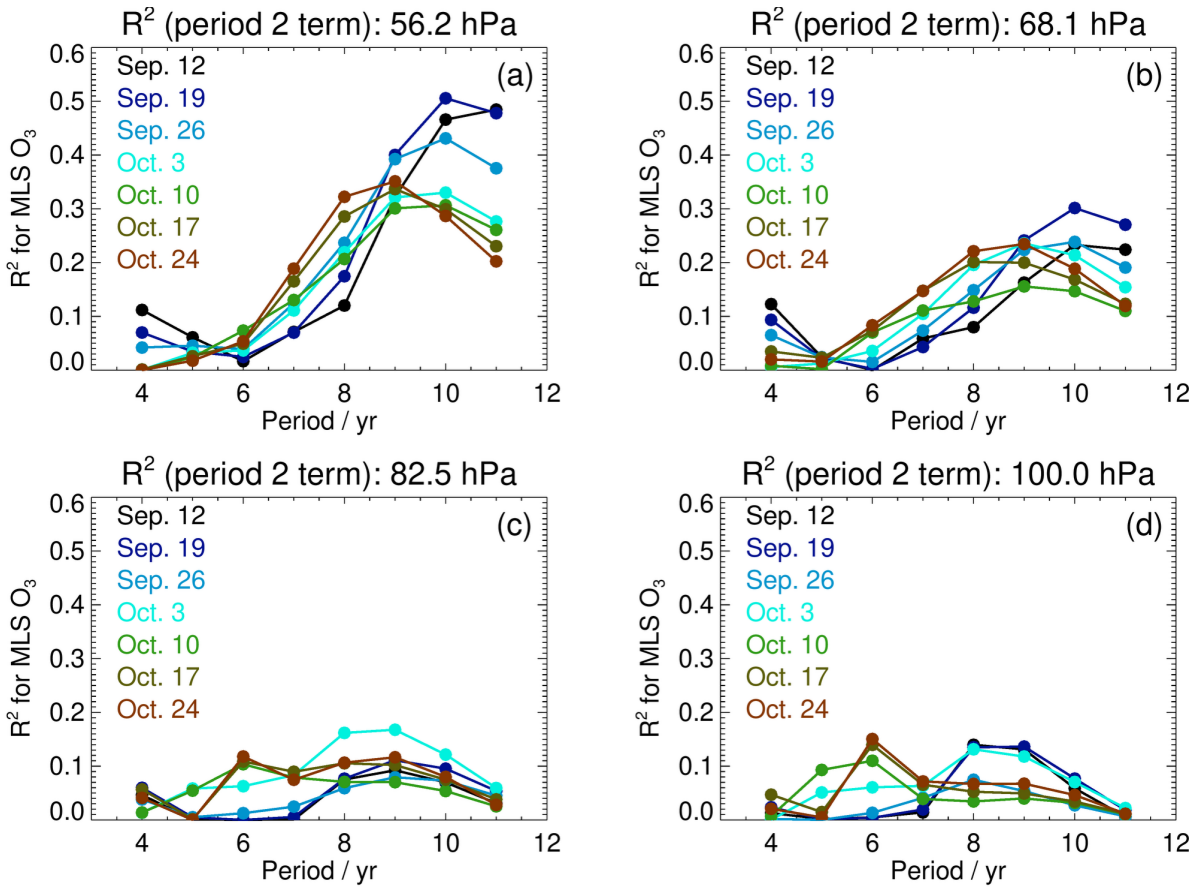

Figure S2. Dependence of R^2 for the period 2 (P_2) component of the MLR fits to the ozone vortex-average time series on the value of P_2 at (a) 56, (b) 68, (c) 82, and (d) 100 hPa for different September and October weeks (see legend).

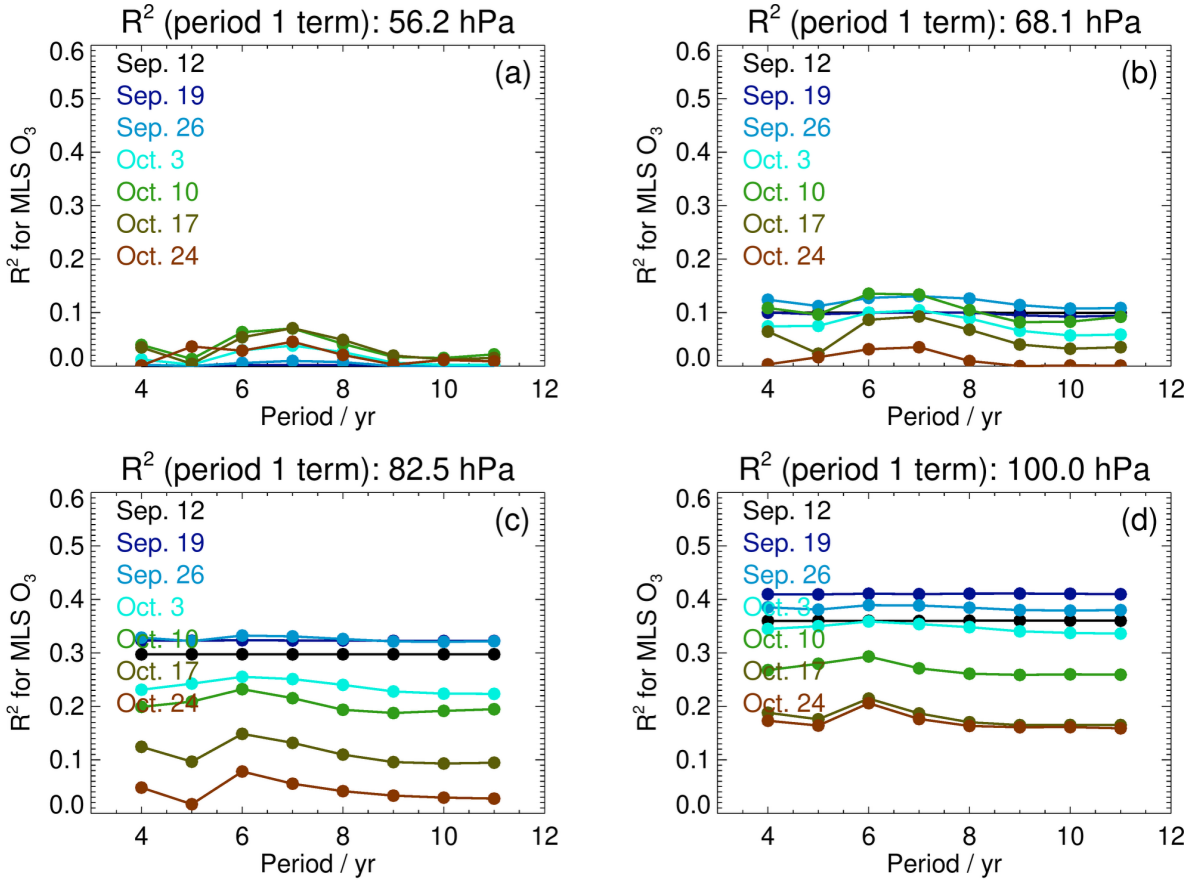

Figure S3. Same as Fig. S2 but for dependence of the period 1 (P_1) component of the MLR fits on P_2.

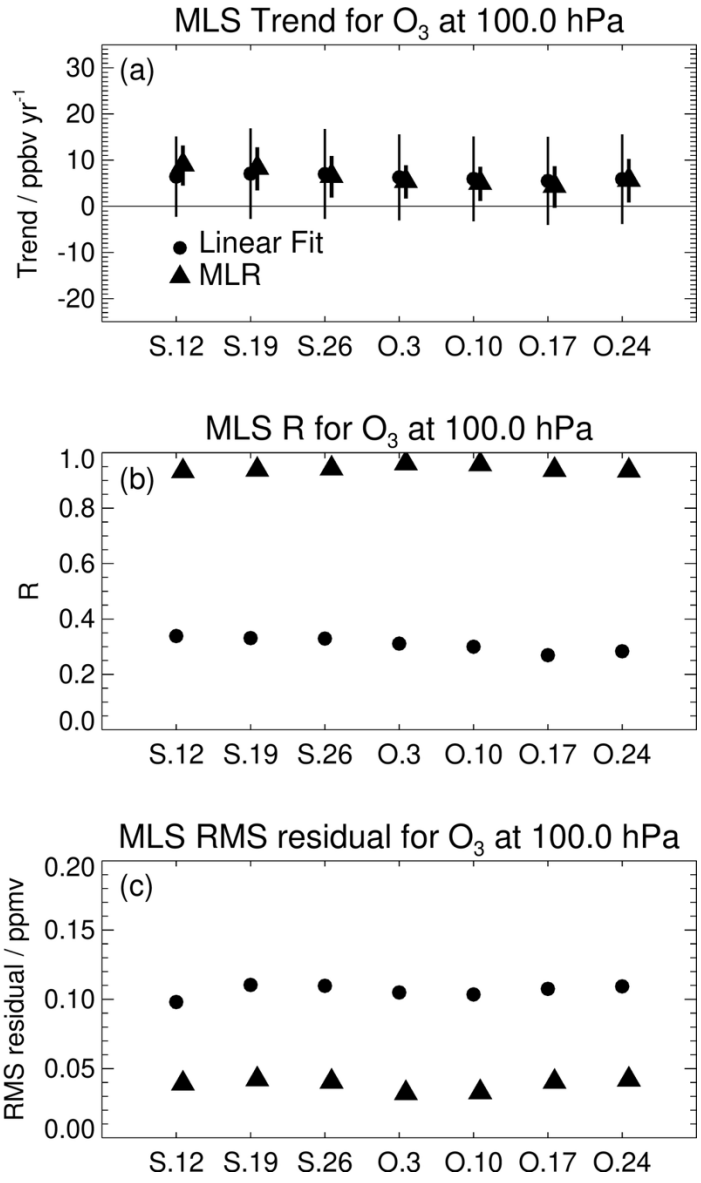

Figure S4. Same as Fig. 12 in the main text, but for the trends and diagnostics of fits to MLS vortex-average ozone series (over 2005–2023) at 100 hPa.

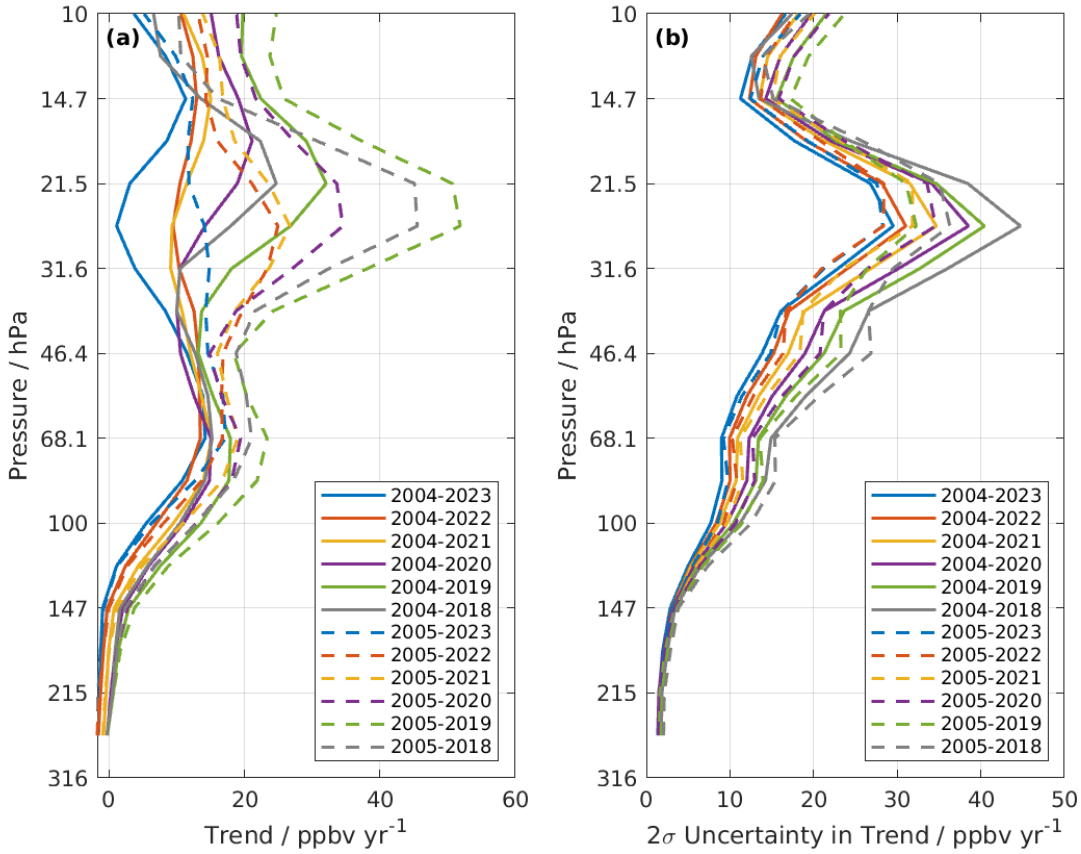

Figure S5. (a) Linear trends from fits to September means of MLS v5 ozone daily vortex averages from the year ranges shown. Solid lines correspond to epochs starting in 2004 and dashed for those starting in 2005, while colors denote the different ending years. (b) 2σ uncertainties in the trends shown in (a).

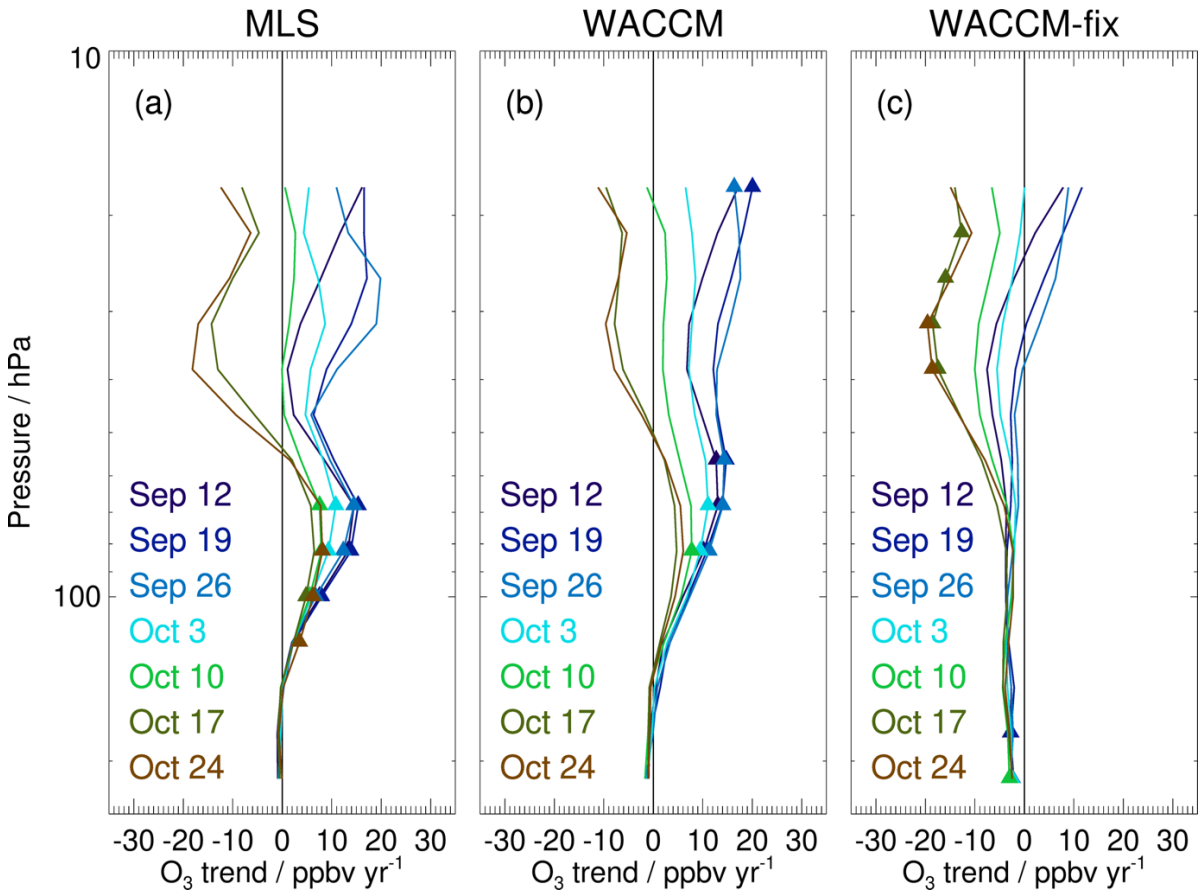

Figure S6. Same as Fig. 17 in the main text, but for trend results obtained with the addition of an AAO index term to the basic MLR analysis (see text) of vortex-average ozone over Antarctica for 2005–2023.

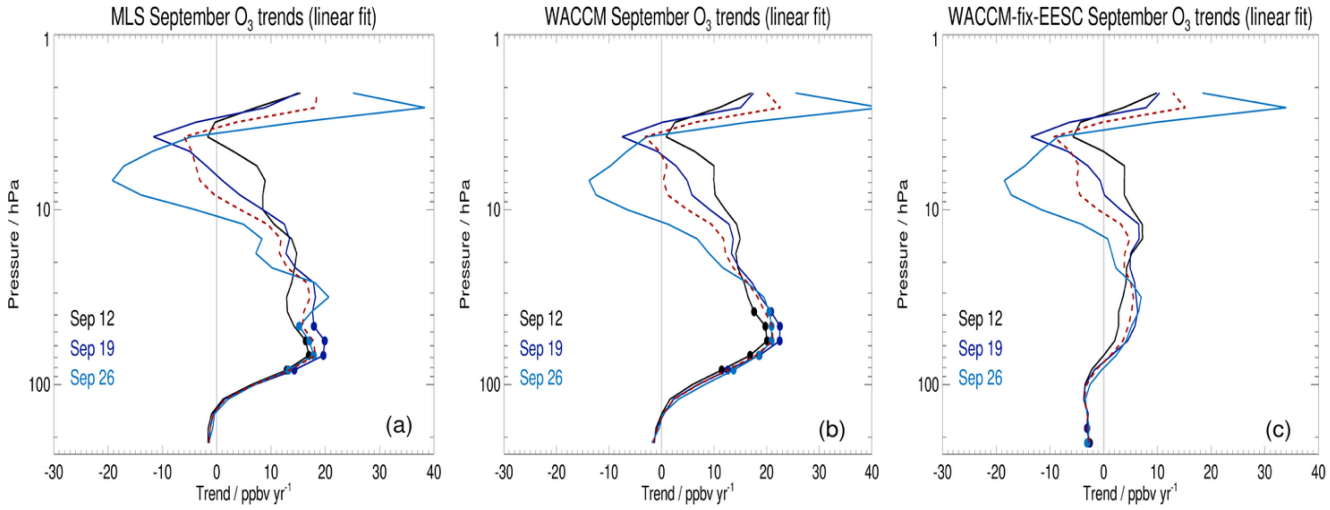

Figure S7. Results from simple linear trends for the lower and upper stratospheric vortex-average ozone change for three weeks in September (see legend) for (a) MLS, (b) WACCM, and (c) WACCM-fix-EESC. The average trend from these three weeks is shown by the red dashed lines. Statistical significance is markedmarked by filled circles when the trend exceeds twice the error in the trend.

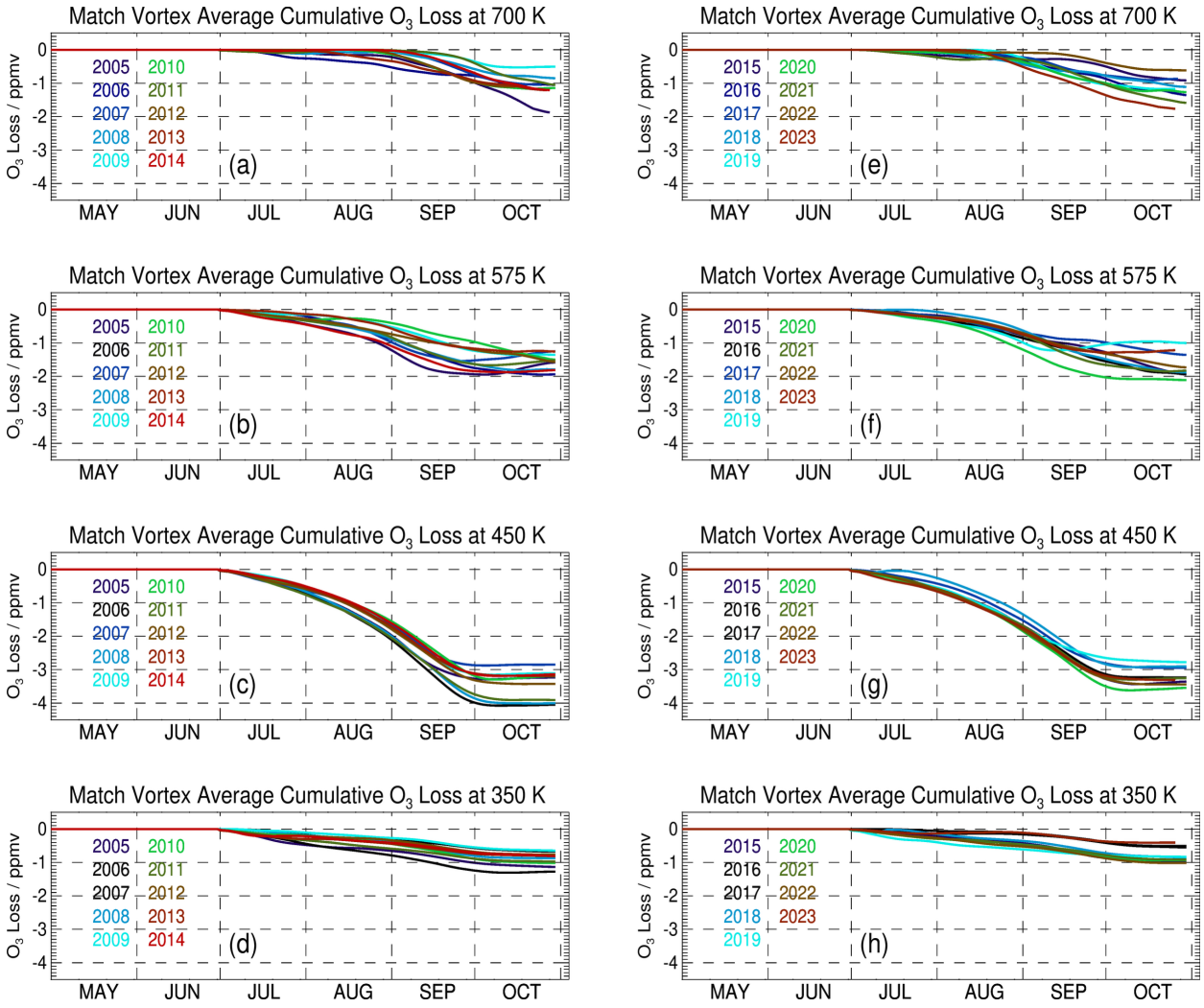

Figure S8. Cumulative ozone losses from the Match technique inside the Antarctic vortex as a function of day, from May to October, at four different θ levels; (a), (b), (c), and (d) show results for 700K, 575K, 450K, and 350K, respectively, for 2005 through 2014, while (e), (f), (g), and (h) show results for the same levels, respectively, for 2015 through 2023.

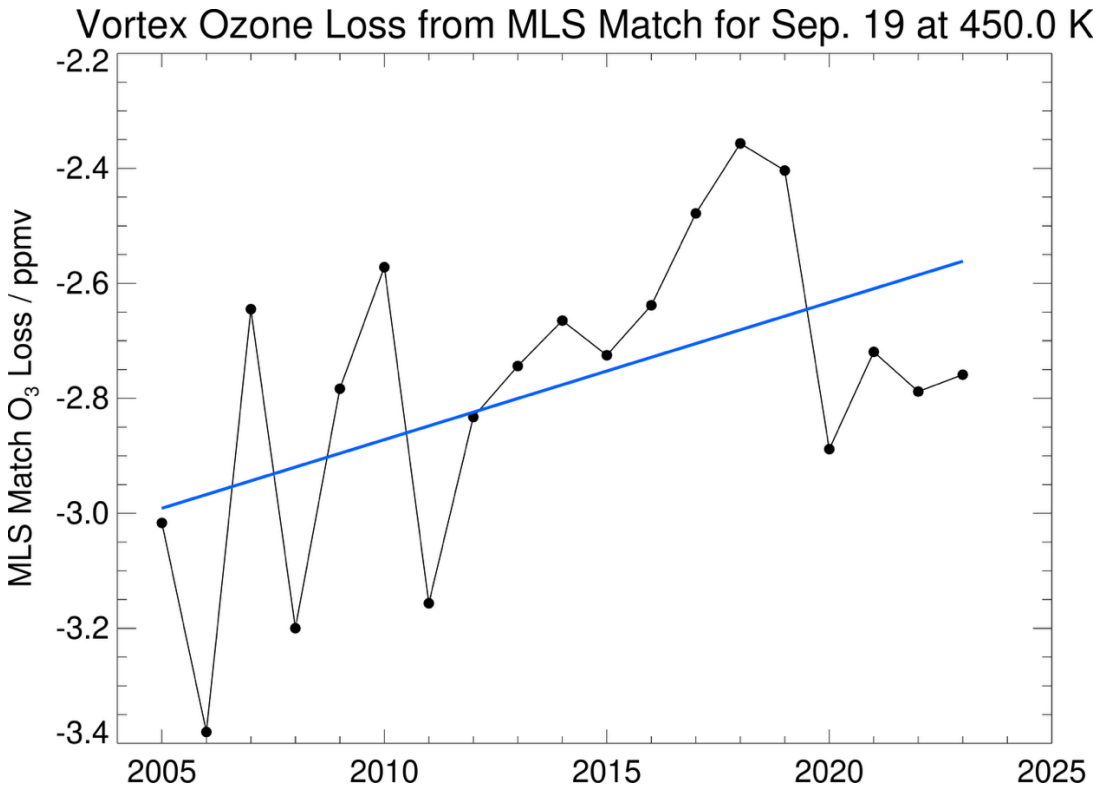

Figure S9. Match-derived weekly average ozone loss values centered on September 19 at 450 K for 2005–2023, based on MLS data inside the Antarctic vortex. The blue line shows a simple linear fit.